UC Berkeley
UC Berkeley Electronic Theses and Dissertations

Title
Mathematical Modeling of Bacterial Motility

Permalink
https://escholarship.org/uc/item/30g1d1n1

Author
Chen, Jing

Publication Date
2010

Peer reviewed|Thesis/dissertation

Mathematical Modeling of Bacterial Motility

by

Jing Chen

A dissertation submitted in partial satisfaction of the

requirements for the degree of

Doctor of Philosophy

in

Biophysics

in the

Graduate Division

of the

University of California, Berkeley

Committee in charge:

Professor George F. Oster, Chair
Professor John C. Neu
Professor Phillip L. Geissler
Professor Daniel A. Fletcher

Spring 2010

Abstract

Mathematical Modeling of Bacterial Motility

by

Jing Chen

Doctor of Philosophy in Biophysics

University of California, Berkeley

Professor George F. Oster, Chair

Bacterial motility is an interesting field of biophysics with many open mysteries. Mathematical models integrate experimental observations into a conceptual framework that elucidates the underlying mechanisms. They also provide physical insight into the general principles that govern the motion, energy conversion, and signal transduction. This thesis summarizes models for two gliding bacteria: mycoplasma and myxobacteria.

The model for mycoplasma motility sheds light on how temperature affects the gliding speed of the cell by influencing the rupture dynamics of motor-substrate adhesion. Mycoplasmas exhibit a novel, substrate-dependent gliding motility that is driven by about 400 "leg" proteins. The legs interact with the substrate and transmit the forces generated by an assembly of ATPase motors. The velocity of the cell increases linearly by nearly 10 fold over a narrow temperature range of 10 – 40ºC. This corresponds to an Arrhenius factor that decreases from ~ 45 k_BT at 10ºC to ~ 10 k_BT at 40ºC. On the other hand, load-velocity curves at different temperatures extrapolate to nearly the same stall force, suggesting a temperature-insensitive force generation mechanism near stall. The model proposes a leg-substrate interaction mechanism that explains the intriguing temperature sensitivity of this motility. The large Arrhenius factor at low temperatures comes about from the additive effect of many smaller energy barriers arising from many substrate binding sites at the distal end of the leg protein. The Arrhenius dependence attenuates at high temperature due to two factors: (1) the reduced effective multiplicity of energy barriers intrinsic to the multiple-site binding mechanism, and (2) the temperature-sensitive weakly facilitated leg release that curtails the power stroke. The model suggests an explanation for the similar steep, sub-Arrhenius temperature-velocity curves observed in many molecular motors, such as kinesin and myosin, wherein the temperature behavior is dominated not by the catalytic biochemistry, but by the motor-substrate interaction.

The model for myxobacteria explains the mechanism of the so-called Adventurous, or A-motility system. A-motility in myxobacteria recruits the bacterial cytoskeleton protein MreB along with proton-driven motors homologous to the stators of the bacterial flagellar motor. This is the first known prokaryotic example where the bacterial cytoskeleton mediates cell motility. The mechanism may be widespread in bacteria, since both MreB homologs and MotA-MotB

homologs are common across a variety of bacterial species. The model introduces cargo-mediated force generation as a key assumption. There are two types of cargo, one causing high drag and the other low drag. They are unequally distributed along the two strands of the double helical track, thereby creating an unbalanced force that drives cell motion. The unequal distribution results from the unequal cargo exchange rates at the cell poles. And these rates are controlled by biochemical oscillators. Besides reproducing the cell velocity and the rotational speed of the track, the model also explains many other experimental observations on myxobacteria motility, including periodic reversals of the cell motion, short pauses before cell reversals, and a whole series of experiments showing the dynamics of motility-related protein clusters at the cell poles and periodically along the substrate interface.

Table of Contents

Acknowledgements

I shall deeply thank Professor George Oster for being a great advisor for me in the past five years. I could not have made through the numerous adversities in my research, as well as those in my life, if he had not shown unchanging support and encouragement at all times.

I shall thank Professor John Neu for all the mathematics he taught me in these projects. And more importantly, his dedication to teaching students is one of the reasons that inspire me to continue academic pursuit after some serious swinging.

I shall thank my parents for their unconditional love and care, and the harbor they provided at my hardest times. The much improved communication with them is the best gift I received in these years.

Last but not least, I shall thank so many of my friends who have shared my joy, excitement, sadness, frustration and growth through the years. They created a warm family for me thousands of miles away from home.

Jing Chen

Education

2010, Ph.D., Biophysics, University of California, Berkeley, USA
- Dissertation: *Mathematical Modeling of Bacterial Motility*

2004, M.S., Mathematics in Bioscience, Technical University of Munich, Germany
- Thesis: *Stability of the Movements of the Elbow Joint*

2002, B.S., Biology, Fudan University, China
- Thesis: *The Complexity Indices of EEG Signals*

Research Experience

Dissertation research with Prof. George Oster   UCB, 2005−10
- Project: *Modeling myxobacteria motility*
- Project: *Modeling mycoplasma motility*
- Constructed, analyzed and simulated mechanochemical models for bacterial motility.

Summer intern at Merck Research Lab   Merck, Co., 2009
- Project: *Parameter estimation in large-scale cardiovascular models using interpolative approximations*
- Programmed for parallel computation with compiled MatLab codes.

Lab rotations (3 labs)   UCB, 2004−05
- Coded Pearl programs for bioinformatics studies.
- Used microscopy to study biological membranes.
- Conducted mathematical analysis of biochemical networks.

Master thesis with Prof. Jürgen Scheurle, Math Dept.   TUM, 2003−04
- Project: *Stability of the movements of the elbow Joint*
- Developed numerical algorithm that maps out the basin of attraction for stable solutions to nonlinear ODE models.
- Applied the algorithm to the analysis of elbow mechanics in human.

Summer research with Prof. Leo van Hemmen, Phys Dept.   TUM, 2003
- Project: *Neuronal model for distance-localizing behavior in sand scorpions*
- Constructed neuronal network model for prey localization in sand scorpions.
- Implemented neuron population model and statistical analysis.

Undergraduate thesis with Prof. Fanji Gu, Biol Dept.   Fudan U, 2002
- Project: *The complexity indices of EEG signals*
- Developed algorithms to evaluate the complexity of EEG signals, and differentiate resting versus thinking states in human subjects.

- Conducted EEG signal recording.

Research assistant with Prof. Ping Xu, Biol Dept.   Fudan U, 2000−02
- Conducted molecular biology experiments to study cancer.

Publications

Chen, Neu, Nan, Zusman and Oster, *A mechanochemical model for A-motility in Myxococcus xanthus: proton-driven motors running on helical cytoskeleton.* (in preparation)

Chen, Neu, Miyata and Oster, *Motor-substrate interactions in mycoplasma motility explain non-Arrhenius temperature dependence*. Biophys. J. 97(11):2930–2938

Xing and Chen, *The Goldbeter-Koshland switch in the first-order region and its response to dynamic disorder.* PLoS ONE. 14(2008): e2140.

Sliusarenko, Chen and Oster. *From biochemistry to morphogenesis in myxobacteria.* Bull. Math. Biol. 68(2005): 1039-1051.

Teaching Experience

Graduate Student Instructor, *Computer simulation in biology* (upper division)   2006−08
- Held discussion sessions, designed and graded homework assignments, revised course materials

Chapter 1   Introduction

Bacterial motility is a fascinating area of biophysics with many unsolved mysteries. Studies in this field lead to potential applications in medicine and engineering. Mathematical modeling is a powerful tool in these studies. It unifies the experimental observations into a conceptual framework to understand the motility process. They also provide physical insight into the general principles that govern the mechanical motion, energy conversion, and signal transduction in the world of microscopic organisms.

1.1   Bacteria motility at a glance

Despite the relative simplicity of their genomes, bacterial cells surpass eukaryotic cells in the diversity of their motility mechanisms. Eukaryotic cells move in two major ways. Most of them crawl by repetitive extension, attaching, retracting, and detaching of pseudopodia or lamellipodia, which are driven by biased polymerization and depolymerization of the cytoplasmic actin network. Some cells swim with cilia or flagella that are constructed from bundles of doublet microtubules (Lodish, Berk et al. 2000).

Bacterial cells, in contrast, have developed various other mechanisms to move. For example, *Escherichia coli* swims by rotating spiral-shaped flagella (Figure 1-1); *Spiroplasma citri* screws through the water by propagating a handedness change down its spiral-shaped body (Figure 1-2) (Shaevitz, Lee et al. 2005); *Pseudomonas aeruginosa* tows itself forward by sending out and retracting type IV pili (Figure 1-3) (Skerker and Berg 2001); *Listeria monocytogenes*, as a parasite, expropriates the host's actin polymerization to propel itself (Figure 1-4) (Cameron, Giardini et al. 2000). This is but a few that have been at least partially understood. Many more types of bacterial motility remain mysterious.
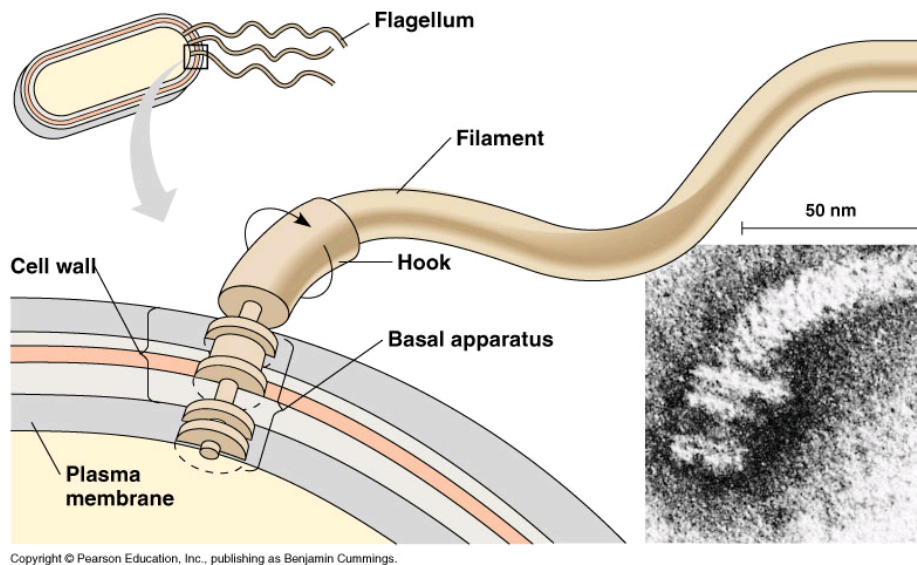
Figure 1-1: *E. coli* rotates spiral-shaped flagella to swim. Downloaded from http://kentsimmons.uwinnipeg.ca/16cm05/1116/16monera.htm.

1
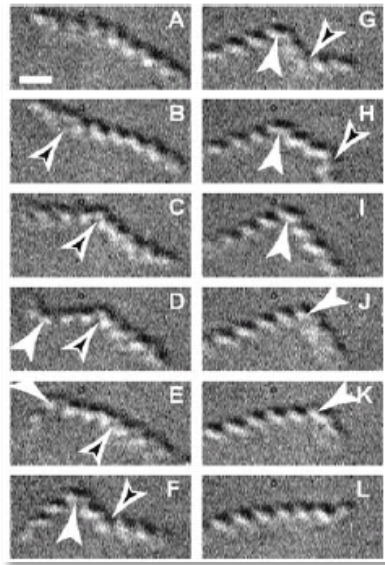
Figure 1-2: *Spiroplasma* swims by propagating a handedness change down the spiral-shaped body. (Shaevitz, Lee et al. 2005)
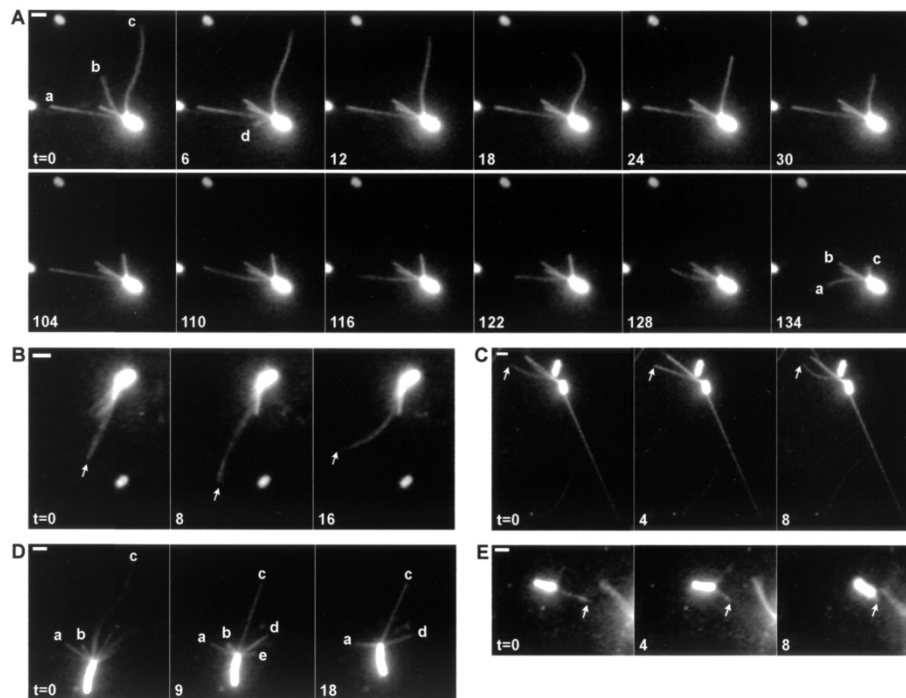
Figure 1-3: *P. aeruginosa* uses type IV pili as towlines (Skerker and Berg 2001).
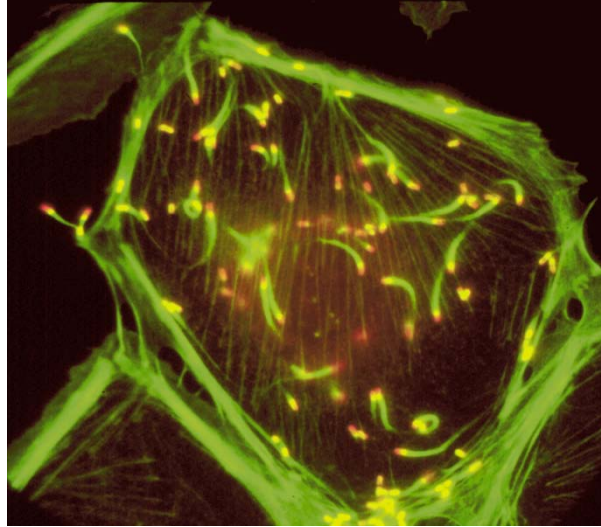
Figure 1-4: *Listeria monocytogenes* triggers actin polymerization in the host cell to propel itself. Green, actin filaments; red, *Listeria*. Downloaded from http://cmgm.stanford.edu/theriot/.

Study of bacterial motility has important biomedical and engineering applications. Knowledge of pathogen motility facilitates the development of new antibiotics that specifically inhibit the spreading of pathogens. Due to the vast diversity of bacterial motility, especially their differences from eukaryotic motility, such medicines may have minimal side effects on human cells, as well as the beneficial bacteria in the human body. Alternatively, bacteria can be used as highly specific drug delivery agents that target directly the site of disease, incurring minimal damage to healthy tissues. Cheap and easy to mass-produce, bacteria are competitive candidates for this purpose. Furthermore, understanding the mechanisms of bacterial motility helps the mimetic design of microscopic machinery. To achieve these ambitions we must first understand how bacteria move.

1.2   Collaboration between modeling and experiments

In the study of bacterial motility, the combined efforts in experiments and modeling often give the best solution to the problem. Experiments define the facts about motility, e.g. the structure and molecular components of the motility apparatus, the force-velocity relationship, etc. Models, on the other hand, weave these facts into a logically integrated picture that explains their dynamical interactions. Unknown aspects of the picture are often momentarily filled in with assumptions that await proof or disproof by further experiments. Many assumptions are not directly testable in experiments, at least with current methods. But predictions stemming from them can serve a constructive purpose indirectly by suggesting future experiments. In this way models play an important feedback role on experiments.

There are many successful models of bacterial motility. The flagella-driven motility in *E. coli* gave rise to the best known models in the field. These models focus on different aspects of the

motility. The biased random walk models explain the emergence of chemotactic behavior (Keller and Segel 1971; Alt 1980); the fluid mechanics models explain the generation of thrust on the cell by rotating the helical flagella (Macnab 1977; Purcell 1997); mechanochemical models explain the generation of rotational torque by the flagellar motor (Xing, Bai et al. 2006; Bai, Lo et al. 2009). Other motility models have been constructed for *Listeria* (Mogilner and Oster 2003), *Spiroplasma* (Jing, Wolgemuth et al. 2009; Wada and Netz 2009), etc.

The focus of the model is usually restricted by the existing experimental observations. Take *E. coli* motility again as an example. The fluid mechanics models came first because it can be sufficiently formulated and analyzed as soon as the rotation of the helical shaped flagella is observed and correlated to the cell motility (Berg and Anderson 1973). Similarly, the run-and-tumble model for chemotaxis was based on the cell-tracking experiments that measure the varied tumble frequencies as the cell goes up or down the nutrient gradient (Berg and Brown 1972). But the flagellar motor itself could not be modeled until the structure and function of its constituent macromolecules can be examined with modern experimental techniques, such as high-resolution electron microscopy and NMR spectroscopy.

Because of the complexity of cell motility and regulation, the effective interplay between modeling and experiments lives in a subtle regime. Ideally, a model gives a creative stretch beyond summarizing the experiments. It would provide no new information if abstraction and assumptions are excluded. But too much of these reduce it to blind guesswork. Thus it is up to the researcher to judge how far the model should go, based on the current state of the experimental knowledge.

1.3   Physical rules in the microscopic world

Due to the microscopic size of the bacterium and its motility apparatus, there are two general physical properties associated with bacterial motility: inertia is negligible and thermal fluctuations are significant. This is true for any moving object of similar size (nm ~ µm) and velocity ($< 10^2$ body sizes per second) in an aqueous medium. Motion on such scales has a negligible Reynolds number (~10^{-6}), which characterizes the ratio between inertial and viscous forces. In this regime, a micron-sized bacterium can only coast for ~0.01 nm or 0.1 µs in water (Purcell 1977). Therefore, inertia can be safely neglected in modeling bacterial motility. That is, a force results in a proportional instantaneous velocity, $F = \zeta V$, instead of an acceleration in Newton's 2nd Law. Here ζ is the hydrodynamics drag coefficient, which depends on the medium, the shape, and the size of the object: ζ ~ (medium viscosity) × (shape) × (size).

On the other hand, microscopic objects are subject to tremendous thermal fluctuations. This is characterized by a large diffusion coefficient, roughly inversely proportional to the size of the object. For example, a micron-sized bacterium in water has a diffusion coefficient ~0.5 µm²/s. Thus the bacterium diffuses by about 1 µm in 1 s (distance² ~ 2 × diffusion coefficient × time), which is comparable to the distance it travels directionally (taking the speed of *E. coli* ~2 µm/s). Because the physical unit of the diffusion coefficient, µm²/s, is different from that of velocity, µm/s, diffusion wins on short time scales, and directional motion wins on long time scales. For a bacterium, the diffusion and the directional motion are commensurable at a time scale on the

4

order of seconds. Yet most biochemical reactions happen on the order of milliseconds or faster. To study motility driven or regulated by such reactions, thermal fluctuations must be considered.

Sometimes thermal fluctuations can be ignored to simplify the mathematical analysis and computation. But the validity of such approximations needs careful evaluation. One typical scenario for the approximation is that a steep energy well constrains the thermal fluctuations within a small range. The object equilibrates to a Boltzmann distribution given by $\exp(-V/k_BT)$, where V is the energy well, k_B is the Boltzmann constant, and T is the absolute temperature. For instance, the secondary structure of a protein is usually molded with strong chemical bonds, essentially deep energy wells. Thus for some purposes we can ignore the internal thermal fluctuations and treat the structure as one unit. Models of bacterial motility often apply such approximations to higher levels, including protein subunits, whole proteins, protein complexes, even the whole cell. Another typical scenario for ignoring thermal fluctuations is when thermal fluctuations cause only a normally distributed deviation around the mean path, and only the mean behavior is of interest. But one should be aware that energy inputs may "color" the thermal noise. In this case the resultant mean behavior differs with or without thermal fluctuations. In extreme cases like polymerization-driven motility (e.g. *Listeria*), the motion is directly driven by thermal fluctuations and rectified, or biased, by chemical reactions (Wang and Oster 2002; Mogilner and Oster 2003). Such motors stall without thermal fluctuations.

1.4 Mechanochemical modeling for bacterial gliding motility

Gliding motility is defined as substrate-dependent propulsion in the absence of obvious external motility organelles, like flagella and pili, or conformational changes in the cell shape, as in *Spiroplasma* (Lawrence and Richard 1971; Burchard 1981). In this work I have modeled the motility of the Mollicute, *Mycoplasma mobile*, and the myxobacterium, *Myxococcus xanthus*. Although both glide on solid surface, their motility mechanisms have almost nothing in common. The mycoplasma is driven by hundreds of tiny rowing "leg" proteins distributed around the neck of the cell, whereas the myxobacterium is driven by motors running along an internal helical cytoskeleton. Other gliding mechanisms were also proposed for different bacteria, e.g. surface waves on the cell envelope (Lawrence and Richard 1971), inchworming (Burchard, Burchard et al. 1977), hydration of secreted slime (Wolgemuth, Hoiczyk et al. 2002).

Mechanochemical models, as the name suggests, encompasses the mechanics, the biochemistry and their interactions. The mechanical motion of the cell is powered by biochemical reactions, typically ATP hydrolysis or transmembrane ion motive force. It is usually signaled and regulated by biochemical reactions, too. On the other hand, recent years have witnessed increasing attention to the regulatory feedback from mechanics to biochemistry. For instance, kinesin walks along the microtubule hand over hand because the ATP binding at the leading head is inhibited by backward tension (Rosenfeld, Fordyce et al. 2003; Hyeon and Onuchic 2007; Gennerich and Vale 2009); the torque generated by the bacterial flagellar motor remains nearly constant up to a "knee" velocity because the ion channel is gated by the mechanical motion (Xing, Bai et al. 2006). The crosstalk between mechanics and biochemistry demonstrates a much more interesting world inside the cells than a well stirred reaction tank, as they used to be treated. Mechanochemical coupling has become more recognized as a general principle involved in every

aspect of cell biology, from enzymatic reaction to cell mitosis. Cell motility provides an excellent platform for studying the principles of mechanochemical coupling.

My models depict coarse-grained systems with small numbers of interacting components. The components are defined according to structural and dynamical information provided by experiments. These models contrast to molecular dynamics (MD) models, a type of model commonly used to study the mechanochemistry of biomolecules. MD models compute the trajectories of all the atoms or small chemical groups in the system, generating results with very high temporal and spatial resolution. Yet the computational cost is formidable. MD models can handle systems up to protein level in size and nanosecond in time – and even this takes CPU-years to compute. Coarse-grained models, by contrast, usually identify no more than a few components. The much reduced modeling scale enables cheap, usually PC-executable computation, even analytical solutions when lucky. Because bacterial motility usually recruits thousands of proteins and the dynamics may occur in seconds or longer, the coarse-grained models have great advantage over the MD models in computational efficiency. Furthermore, the MD models require detailed information about the molecular structure, which is often not available for some or all the relevant components of the system. But coarse-grained models only resolve how the components interact with each other, and do not care about their detailed structure unless necessary for the function. Thus the coarse-grained models can be constructed on much less experimental data.

Albeit leaving out a lot of information compared to MD models, the coarse-grained models try to capture the most relevant and essential features in the motility process. This is possible mainly thanks to the separation of temporal and spatial scales, especially the time scale separation. Given a major time scale of interest, processes on much longer time scales can be treated as quasi-steady, and those on much shorter time scales can be assigned equilibrium distributions. For example, in the study of bacterial motility with time scales of milliseconds to seconds, protein synthesis takes much longer and thus protein concentrations are often assumed constant; the fluctuations of protein conformation is much faster and are usually treated as an ensemble average with Gaussian noise. Similar approximations apply to the spatial dimension. For instance, the surface geometry of a protein on the atomic scale is negligible in estimating the protein's hydrodynamic drag coefficient. Such approximations keep the model focused on the essential features. Last but not least, it is much easier for the human mind to grasp physical insights from only a handful of interacting parts. So the coarse-grained model provides a great platform for studies of principles.

6

Chapter 2   Mycoplasma Motility

Mycoplasmas exhibit a novel, substrate-dependent gliding motility that is driven by about 400 "leg" proteins. The legs interact with the substrate and transmit the forces generated by an assembly of ATPase motors. The velocity of the cell increases linearly by nearly 10 fold over a narrow temperature range of 10–40ºC. This corresponds to an Arrhenius factor that decreases from ~45 k_BT at 10ºC to ~10 k_BT at 40ºC. On the other hand, load-velocity curves at different temperatures extrapolate to nearly the same stall force, suggesting a temperature-insensitive force generation mechanism near stall. We propose a leg-substrate interaction mechanism that explains the intriguing temperature sensitivity of this motility. The large Arrhenius factor at low temperature comes about from the addition of many smaller energy barriers arising from many substrate binding sites at the distal end of the leg protein. The Arrhenius dependence attenuates at high temperature due to two factors: (1) the reduced effective multiplicity of energy barriers intrinsic to the multiple-site binding mechanism, and (2) the temperature-sensitive weakly facilitated leg release that curtails the power stroke. The model suggests an explanation for the similar steep, sub-Arrhenius temperature-velocity curves observed in many molecular motors, such as kinesin and myosin, wherein the temperature behavior is dominated not by the catalytic biochemistry, but by the motor-substrate interaction. This work was published in Biophysical Journal 97(11):2930–2938 (Chen, Neu et al. 2009).

2.1 Introduction

Mycoplasmas are a genus of wall-less bacteria with compact genomes that may have arisen as a result of retrograde evolution (Razin, Yogev et al. 1998). They are the smallest known free-living, self-replicating organisms. Despite the loss of many biological functions, mycoplasmas demonstrate a novel gliding motility on solid substrates, such as glass, plastic and surface of epithelial cells (Rosengarten, Fischer et al. 1988; Kirchhoff 1992; Miyata 2005). Their locomotion is always in the direction of a characteristic membrane protrusion at one pole of the cell (the "nose") (Seto, Layh-Schmitt et al. 2001; Miyata and Uenoyama 2002; Kenri, Seto et al. 2004; Henderson and Jensen 2006). The motility mechanism is novel. The mycoplasma genome contains no homologs to genes associated with known mechanisms of bacterial motility (Fraser, Gocayne et al. 1995; Himmelreich, Hilbert et al. 1996; Chambaud, Heilig et al. 2001; Jaffe, Stange-Thomann et al. 2004).

The motility studies are carried out mainly on the fastest gliding species, *Mycoplasma mobile*. Under lab conditions, *M. mobile* glides smoothly and continuously on glass surface with velocities of 2.0−4.5 μm/s, or 3−7 body-lengths/s (Rosengarten and Kirchhoff 1987). The energy source is ATP hydrolysis (Jaffe, Miyata et al. 2004; Uenoyama and Miyata 2005; Ohtani and Miyata 2007). Recent experiments reveal a complicated motility organelle in its nose (Nakane and Miyata 2007). The core of the organelle consists of a dock structure fixed at the distal end of the nose, and dozens of filaments extending radially from the dock. These filaments anchor about 400 single protein "legs" that protrude through the cell membrane and interact with the substrate (Figure 2-1)(Miyata and Petersen 2004; Uenoyama, Kusumoto et al. 2004; Metsugi, Uenoyama et al. 2005; Adan-Kubo, Uenoyama et al. 2006; Uenoyama, Seto et al. 2009). Since the leg is the

best studied protein in the complicated organelle, our model focuses on how these legs harness the forces generated by the ATPase motors to drive the motion of the cell.

M. mobile shows intriguing velocity changes with temperature and load force. The temperature-velocity curve is steep and sub-Arrhenius. The velocity increases almost linearly by about 10-fold over a narrow temperature range from 10ºC to 40ºC (Figure 2-3A) (Miyata, Ryu et al. 2002). Translated onto a $1/T \sim \log V$ plot (circles in Figure 2-3B), these data correspond to an Arrhenius factor that decreases from ~45 k_BT at 10ºC to ~10 k_BT at 40ºC. On the other hand, the velocity decreases nearly linearly with increasing load force, but the stall force extrapolates to ~25 pN at different temperatures (c.f. fig.4 in (Miyata, Ryu et al. 2002)). Cells attached to micro-beads trapped by optical tweezers also stall when pulled by a force of ~25 pN (Miyata, Ryu et al. 2002). These data suggest that the force generation step is insensitive to temperature near stall loads.

Here we propose a leg-substrate interaction mechanism to explain the non-Arrhenius temperature dependence of mycoplasma motility. In this mechanism the release of the leg from the substrate is the major temperature-sensitive factor. Soo and Theriot (Soo and Theriot 2005) suggested in their model for *Listeria* motility that the large Arrhenius factor for the cell velocity is caused by the cooperative breaking-off of multiple binding sites so that the Arrhenius factors of single sites add. Our model goes further and explains the decrease in the Arrhenius factor as temperature rises, i.e. the sub-Arrhenius relationship between temperature and velocity. The model can be generalized to explain similar temperature sensitivity observed in many "walking" molecular motors such as kinesin and myosin (Anson 1992; Bohm, Stracke et al. 2000). This theory reveals the motor-substrate interaction, especially the unbinding process, as the dominant factor affected by temperature, albeit not in a simple Arrhenius fashion.
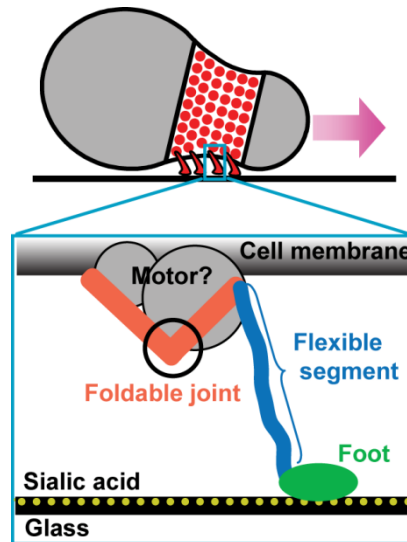

Figure 2-1: Motility apparatus of *M. mobile*. 400 leg proteins are located at the neck of the *M. mobile* cell. Each leg assumes a music-note-like shape (*zoom-in view*), with two arms at the proximal end, a long flexible segment (*blue*) and a foot (*green*) that interacts with the substrate.

8

2.2 Model and results

In the following sections, we first lay down the framework for the motility process and the basic assumptions used in our model. After that we go into the details of the leg-substrate interaction. In particular, we show that the multiple substrate-binding sites on the leg contribute to the steep, sub-Arrhenius temperature-velocity curve. In addition, we rectify the remaining deviation of the results at high temperatures by the weakly-facilitated foot release during the power stroke. Finally, we show that the resultant load-velocity curve fits with the experimental data and explains the dynamical trajectories observed in optically trapped mycoplasma cells, as well as the temperature-insensitive stall force.

Leg cycle

The geometric shape of the leg protein in mycoplasma has been deduced from electron microscopy studies. The protein looks like a music note (Figure 2-1; see also fig.9 in (Adan-Kubo, Uenoyama et al. 2006)). The two short arms at the proximal end assume an open or a closed conformation, suggesting that the opening and closing motion is driven by the ATPase motor (Ohtani and Miyata 2007). The distal end bulges into a "foot" that interacts with the negatively charged substrate through multiple basic amino acids. The proximal arms and the foot are connected by a long segment. Atomic force microscopy experiments suggest that this long segment is quite flexible (Miyata 2007), so that its mechanical property resembles that of a rope, i.e. exerting much less resistance to being compressed than being stretched.

Based on the structure of the leg protein and the proposed motility mechanism in (Miyata 2008), we modeled the mechanochemical cycle of a single leg as shown in Figure 2-2A.

The mechanochemical cycle begins with the leg in the front position and the foot bound to the substrate. When ATP loads into the motor, the motor carries out a power stroke and pulls on the foot. This process exerts a forward force on the cell body. After the power stroke, the cell continues moving forward, driven by the collective work of the other legs. The foot lags behind. The long segment becomes slack and exerts no force until the foot reaches the backward position and re-stretches the long segment. The long segment pulls the foot off the substrate. Then the leg resets to the front position, the foot rebinds to the substrate and the cycle repeats. We impose the kinematic constraint that the cell moves relative to the substrate with a constant velocity *V*. This simplifies the mathematical analysis, and is justified by the large number of legs and consequent small fluctuations in the velocity of the cell.

In such a system with many degrees of freedom, it is natural to have other pathways on the complicated energy landscape. What we proposed above is the main pathway that most legs follow. In order for this cycle to dominate over the other pathways, the following assumptions must hold:

1. The hinge connecting the proximal arm and the long segment is weakly elastic, with its rest state in the front position. This provides the resetting force for the leg.

2. The motor can bind ATP only after the leg fully resets to the front position. It can be explained by hidden coordinates for the motor (see Appendix A). This assumption, together with the next one, ensures that the power stroke always starts from the front

9

position. This is for analytical convenience, and does not change the essential features of the model.

3. The foot only rebinds to the substrate after it fully resets to the front. We picture the long segment behaving like a Venetian blind: the long segment kinks easily under a backward force and the kink propagates down towards the foot while the segment resets to the front position (leftmost panel of Figure 2-2A). During resetting, the kink keeps the foot in an unfavorable angle to the substrate, preventing its binding until the resetting completes. During the power stroke, however, the segment is unbent because it is under tension.

4. The foot releases more easily when it is pulled forward after the power stroke (steps 3 in Figure 2-2A). This is because the long segment is attached to the posterior end of the foot so that it imposes a peeling force when it pulls the foot forward, as shown in Figure 2-2B. This mechanical asymmetry is necessary for net forward motion.
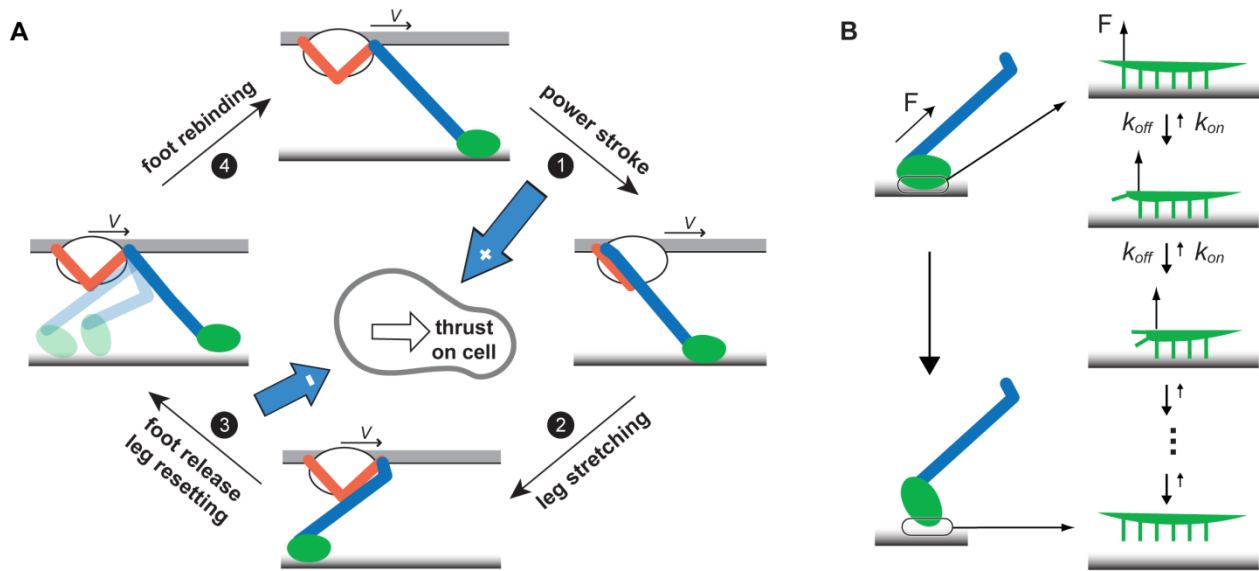
Figure 2-2: Mechanochemical model of a single leg protein. (**A**) Mechanochemical cycle of the leg. The leg starts in the front conformation with the foot bound to the substrate. As ATP zippers into the catalytic site, the motor carries out a power stroke, pulling the cell forward. After the power stroke, the cell continues moving forward at constant velocity V, driven by the collective action of the other legs. The foot lags behind until the long segment is once again in tension. Acting on one end of the foot, the tension helps peel the foot off the substrate. The system must wait for the foot to release from the substrate so that the leg can reset to the front conformation, allowing the motor to bind ATP once again. The cycle repeats as the foot rebinds to the substrate. ATP binding and foot rebinding are assumed to happen very fast, thus not resolved in the analysis. During the cycle, the power stroke applies a positive force on the cell body and the foot tethered beyond its backward re-stressed position, applies a negative force (*blue arrows*). (**B**) Mechanism of foot peeling. The foot interacts with the sialic acids in the substrate through multiple binding sites. The bonds are shown by green projections in the zoom-in

10

view on the right. When the stretched intermediate segment pulls on the foot from one end, most of the tension is exerted on the front-most bond and thus significantly facilitates its unbinding, analogous to peeling off a Velcro strip. In the idealized case, the bonds break off sequentially, forming a Markov process as shown in the sequence of events on the right. The Markov process gives an average peel-off rate of the foot as in Eq.(2.2).

The velocity of the cell is computed from the force balance on the legs. Since inertial forces are negligible at such low Reynolds number, the load force and hydrodynamic drag force on the cell body is equal to the total force generated by the motility organelle. The estimated hydrodynamic drag on the micron-sized cell body moving with a velocity of ~1 μm/s is ~10^{-2} pN, much smaller than the scale of the external load force applied in the experiments; thus it can be neglected. The motility organelle generates forces mainly by two steps in the leg cycle: the power stroke generates a positive force and the foot tethered beyond the backward re-stressed position imposes a negative force. During the re-stretching and resetting steps, the only force is the weak elastic resetting force, which we treat as negligibly small. Intuitively, the force balance at all times ensures the balance of the ensemble average force; and the latter is equivalent to the balance of force impulses. Thus the force balance can be conveniently expressed as an impulse balance:

load force × cycle period =
 # legs × (impulse from power stroke – impulse from tethered foot)

In Appendix D we derive the full version of the force balance equation from the transport equations for the density of feet. These equations can be reduced to the above equation when we neglect the hydrodynamic drag forces and consider the high velocity case.

At zero load, the two impulses on the right hand side cancel, leading to Eq.(2.1). Here V is the velocity of the cell, f_m the motor force, λ the power stroke length, κ the elastic constant of the intermediate segment, and the R_p the peel-off rate of the foot. The computation of R_p leads to the most important conclusion of this work and will be discussed in detail in the following section. On the left hand side of Eq.(2.1), λ/V is the mean residence time of the foot in the power stroke. So the mean impulse delivered by a single foot in one power stroke is $f_m\lambda/V$. On the right hand side, V/R_p is the average stretching of foot from the backward re-stressed position, and thus, $\kappa V/R_p$ is the average force acting on the backward foot. Since the lifetime of backward bound state is $1/R_p$, the impulse delivered per foot in this part of the cycle is $(\kappa V/R_p) \times (1/R_p) = \kappa V/R_p^2$.

$$f_m \frac{\lambda}{V} = \frac{\kappa V}{R_p^2} \quad \Rightarrow \quad V = \sqrt{\frac{f_m \lambda}{\kappa}} R_p \tag{2.1}$$

Eq.(2.1) shows that the unloaded velocity is proportional to the peel-off rate of the foot. The temperature dependence of the velocity follows that of the peel-off rate, as we show in the following that terms under the square root are approximately temperature invariant. The power stroke length, λ, is determined by the geometry of the motor and the leg, and should not change significantly with temperature. The motor force depends on temperature approximately linearly, i.e. $f_m \simeq \Delta G/\lambda = (\Delta H - T\Delta S)/\lambda$; it changes by about 10% over the temperature range of 10°C − 40°C, far from enough to account for the 10-fold increase in velocity. The elastic constant of the

11

stretched leg, κ, depends on the configuration of the intermediate segment. Using the same argument for the motor force, the elastic constant resulting from the entropic part of the spring is a linear function of temperature (Howard 2001), and does not change much in the relevant temperature range. The enthalpic part of the spring is usually attributed to chemical bonds. Since the enthalpy of a chemical bond is generally insensitive to temperature, so is the resultant spring constant.

In the next section we will derive the temperature dependence of the foot peel-off rate with an embedded submodel of the foot-substrate interaction. The submodel explains the steep, sub-Arrhenius temperature-velocity curve, except for some deviation in the high temperature regime.

Foot-substrate interaction

We now consider the foot-substrate interaction in more detail. This is the core part of the model, which explains the steep, sub-Arrhenius temperature-velocity curve.

The foot anchors to the negatively charged sialic acids in the substrate (Nagai and Miyata 2006). The C-terminal domain of the leg protein, which constitutes the bottom part of the foot, contains multiple positively charged amino acids (18 Arg, 21 Lys). It is likely that specific binding sites for sialic acid form around these basic amino acids. Previous studies on the sialoadhesin receptor shows that the sialic acid binding site consists of two key amino acids with positive charges (May, Robinson et al. 1998). This gives an estimate of < 20 binding sites on the foot of mycoplasma, based on which we used 10 in our model. That is, the foot is modeled as an anchoring strip with 10 sites that holds on to the substrate.

The asymmetric geometry of the leg protein suggests that the foot releases from the substrate more easily when pulled forward instead of backward. A backward pulling force, as that during the power stroke, is distributed almost equally amongst all the binding sites. A forward force, however, is concentrated mostly on the rearmost site, largely facilitating its unbinding. After the rearmost site unbinds, the next one undertakes most of the external force and unbinds quickly; and it goes on until all sites unbind. This process is analogous to peeling off a Velcro strip from one end to the other — by contrast it is much harder to rip off the Velcro by exerting an evenly distributed force on it.

The peeling off of the foot can be modeled by a Markov process as shown in Figure 2-2B. Since the rearmost binding site is much more likely to unbind, the unbinding of different sites takes place approximately sequentially. Let Q be the number of binding sites. The corresponding Markov process consists of $Q+1$ states, each indicating the order of the current rearmost bound site, plus the "all-off" state.

$$Q \underset{k_{on}}{\overset{k_{off}}{\rightleftarrows}} Q-1 \underset{k_{on}}{\overset{k_{off}}{\rightleftarrows}} \cdots \underset{k_{on}}{\overset{k_{off}}{\rightleftarrows}} 1 \underset{k_{on}}{\overset{k_{off}}{\rightleftarrows}} 0 \text{ (all-off)}$$

If the on and off rates of all binding sites are identical, the derivation presented in Appendix B gives the peel-off rate of the whole foot as:

$$R_p = k_{off} \times \frac{(1-K)^2}{Q-(Q+1)K+K^{Q+1}} \tag{2.2}$$

where $K = k_{on}/k_{off}$ is the binding constant of a single site. As temperature increases, the enhanced thermal fluctuations facilitate the unbinding, thus decreasing the binding constant, K. Eq.(2.2) satisfies the following properties:

- Low temperature limit: $K \to \infty \Rightarrow R_p \to k_{off}/K^{Q-1}$;
- High temperature limit: $K \to 0 \Rightarrow R_p \to k_{off}/Q$.

If the binding constant, K, depends on temperature in an Arrhenius way, then in the low temperature limit, the Arrhenius factor of the foot peel-off rate, R_p, is approximately the Arrhenius factor of K multiplied by the number of sites. This multiplicity effect, however, attenuates as temperature increases; eventually, the effective Arrhenius factor tends to approximately the Arrhenius factor of K at the high temperature limit.

The feature of the model discussed so far leads to the steep, yet sub-Arrhenius temperature dependence of the velocity (dashed line in Figure 2-3A). Data fitting gives the values of the single site rates, k_{on} and k_{off}, as listed in Table 2-1. Figure 2-3B compares the Arrhenius plot of the single-site unbinding rate, the whole-foot release rate, and the temperature-velocity data. Each site bears a factor of 10 k_BT (Table 2-1). But the Arrhenius factor of the whole-foot rate amounts to ~45 k_BT at 10ºC, and attenuates to ~10 k_BT at 40ºC.

Weakly-facilitated foot release during the power stroke rectifies the high-temperature curve

During the power stroke, the foot may also release from substrate. This foot release rate is much smaller than the peel-off rate at low temperature, but becomes significant as temperature increases. In this case all the binding sites share the burden of the motor force. With much weaker facilitation than in the peel-off case, the energy barrier to break the binding of a site remains high and thus the unbinding rate bears a much larger Arrhenius factor. As a consequence, the overall foot release rate increases acutely with temperature (Figure 2-3C).

The foot release curtails the power stroke, and consequently reduces the velocity. This is shown by the velocity dependence in Eq.(2.3). Here R_{wf} denotes the weakly-facilitated foot release rate.

$$f_m \frac{1-\exp\left(-R_{wf}\lambda/V\right)}{R_{wf}} = \frac{\kappa V}{R_p^2} \quad \Rightarrow \quad V = \frac{1-\exp\left(-R_{wf}\lambda/V\right)}{R_{wf}} \frac{f_m}{\kappa} R_p^2 \tag{2.3}$$

The fractional term on the left-hand side of Eq.(2.3) stands for the average duration of the effective power stroke. It is computed from

$$\int_0^{\lambda/V} t f(t;R_{wf})dt + \int_{\lambda/V}^\infty f(t;R_{wf})\lambda/V dt$$

where $f(t;R_{wf})$ is the probability density function of the exponential distribution. Eq.(2.3) tends to Eq.(2.1) in the limit $R_{wf} \to 0$, i.e. when the weakly-facilitated foot release rate is negligibly small. Because the weakly-facilitated rate increases sharply with increasing temperature, its effect on velocity dominates at high temperature. This is the other feature of the model that rectifies the temperature-velocity curve at high temperatures (solid line in Figure 2-3A).

13
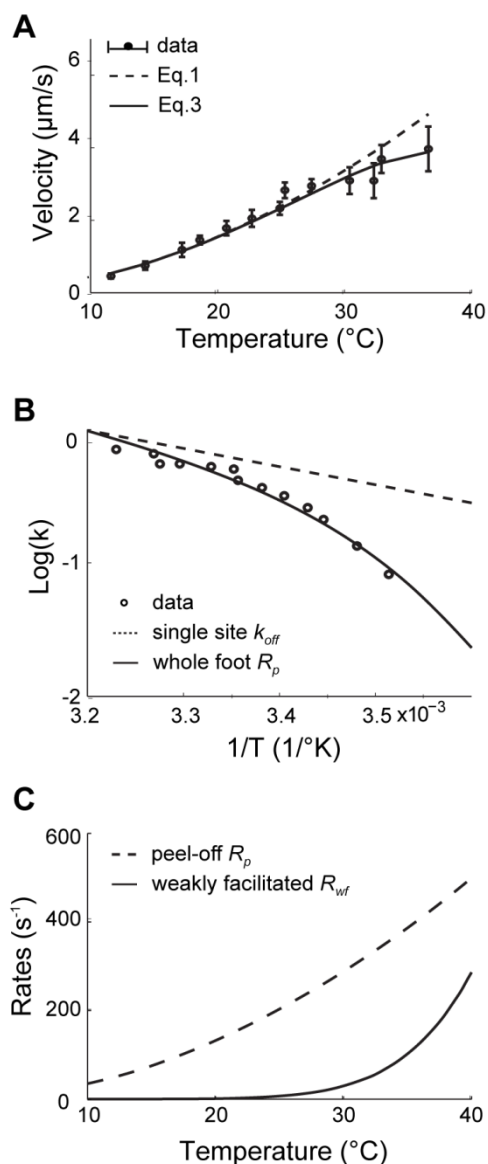
Figure 2-3: Temperature-velocity results. (**A**) Temperature vs. velocity curve. Circles and error bars show the experiment data (taken from (Miyata, Ryu et al. 2002)); the dashed line is the fitting of the model without weakly facilitated foot release during the power stroke using Eq.(2.1); the solid line shows the result with weakly facilitated foot release during power stroke using Eq.(2.3). The effect of weakly facilitated foot release becomes significant at high temperatures, and corrects the deviation from the data. (**B**) The Arrhenius plots of the foot rates and of the data. For comparison, the rates have been multiplied by corresponding constants to level the logarithm plots at the left end. The whole foot peel-off rate, R_p, has a much larger Arrhenius factor than the off rate of a single site does because of the multiplying effect shown in Eq.(2.2). Also, the Arrhenius factor of R_p decreases as temperature increases. (**C**) The peel-off rate R_p and weakly

facilitated release rate R_{wf}. The weakly facilitated rate becomes significant around 25ºC, resulting in the attenuation of velocity at high temperatures.

Table 2-1: List of parameters.

Parameters	Values	Physical meaning	Sources / reasons
N	100	number of legs	out of a total of 400 legs, 1/4 face the substrate
Q	10	number binding sites on each foot	structural information: number of charges on the foot
f_m	0.39 pN	motor force	fitting Eq.(2.1) and Eq.(2.2) with T-V data
λ	28 nm	power stroke length	structure of leg protein: 90º conformational change between two arms of 20 nm
κ	80 pN/μm	elastic constant of intermediate segment	physiological range
k_{on}, k'_{on}	2.9×10^3 s^{-1}	binding rate of single site	fitting Eq.(2.1) and Eq.(2.2) with T-V data, assuming that the on rates are not affected by external force
k_{off}	4.2×10^3 s^{-1} * ($10.6\ k_B$T)	peel-off rate of single site (and its Arrhenius factor)	fitting Eq.(2.1) and Eq.(2.2) with T-V data
k'_{off}	1.9×10^3 s^{-1} * ($16.8\ k_B$T)	weakly-facilitated release rate of single site (and its Arrhenius factor)	fitting Eq.(2.1) and Eq.(2.2) with T-V data

* The rates are listed as their values at the reference temperature 22.5ºC.

The weakly facilitated foot release also corresponds to a Markov process. The Markov states stand for the number of binding sites currently bound. Since the pulling force is almost evenly distributed on the binding sites in this case, the sites do not have to unbind sequentially. Thus the forward rate from state i to i-1 equals ik'_{off} to account for the fact that every bound site has an equal chance to unbind. Similarly the backward rate from state i to i+1 equals $(Q-i)k'_{on}$.

$$Q \underset{k'_{on}}{\overset{Qk'_{off}}{\rightleftharpoons}} Q-1 \underset{2k'_{on}}{\overset{(Q-1)k'_{off}}{\rightleftharpoons}} \cdots \underset{(Q-1)k'_{on}}{\overset{2k'_{off}}{\rightleftharpoons}} 1 \underset{Qk'_{on}}{\overset{k'_{off}}{\rightleftharpoons}} 0 \text{ (all-off)}$$

With the derivation given in Appendix C, we obtain the weakly-facilitated foot release rate as Eq.(2.4). It is computed with k_{on}' and k_{off}' given in Table 2-1.

$$R_{wf} = \frac{Q k_{on}'}{\left(1 + k_{on}'/k_{off}'\right)^Q - 1}$$

(2.4)

As in Eq.(2.2), we see that the exponential term in Eq.(2.4) also brings about the multiplicity of the Arrhenius factor for the single-site binding constant.

This newly introduced detail of the model reduces the calculated velocity significantly for temperatures above 25°C (solid line in Figure 2-3A). With much smaller facilitating force, the energy barrier associated with the unbinding of each site is larger, at 17 k_BT (Table 2-1). Consequently, the weakly-facilitated rate rises sharply starting around 25°C (Figure 2-3C). Nevertheless, it is smaller than the peel-off rate because of less facilitation.

The load-velocity curve explains the dynamical trajectory

In this section we show an interesting hysteresis behavior in the load-velocity curve at low velocities. This leads to an explanation for the dynamical trajectory observed in optical trap experiments.

The calculated load-velocity curve of the model fits with the experiment data (Figure 2-4A). Our calculation extends beyond the range of the data to the low velocity and negative velocity regimes. In the calculation we introduce a spontaneous foot release from the substrate during the re-stretching step at a small, yet finite rate. The spontaneous foot release is a natural consequence of thermal fluctuations. Without any external help, the rate of spontaneous release is even smaller than that of the weakly-facilitated release. The rate is calculated with the same formula as the weakly facilitated release, except for a smaller single-site release rate (Table 2-2 in Appendix D). At large cell velocities, the foot translates backwards fast enough to re-stretch the leg, before which the spontaneous release almost never has a chance to occur. Therefore, the spontaneous release does not play a role when cell velocity is high. Near stall (i.e. zero velocity), however, spontaneous foot release is frequent. This circumvents the peel-off of the foot and reduces its negative impulse. The enhanced model is formulated via transport equations in Appendix D.

The load-velocity curve displays hysteresis: it 'turns around' at a low positive velocity that depends on temperature, and returns in the negative velocity regime. The hysteresis occurs because the power stroke is more often curtailed by weakly-facilitated foot release at low velocities, leading to a loss of traction. Since the rate of weakly-facilitated foot release increases as temperature rises, the hysteresis velocity also increases accordingly.

The stall force changes with temperature much less than the unloaded velocity. At very low velocity the peel-off is interrupted by the spontaneous foot release. Therefore, the average force contributed by a foot in an average cycle is approximately the motor force multiplied by the fraction of cycle period spent in the power stroke. The motor force is insensitive to temperature, as discussed previously. The fraction of power stroke time apparently does not change too much with temperature, either (solid line in Figure 2-5B). So the stall force appears insensitive to temperature.

16

However, the stall force predicted by the model is somewhat smaller than the stall force measured by the optical trap experiment. This may be due to the approximation that, during the peel-off, the unbinding rates of all the binding sites are assumed to be identical. In reality, the unbinding rates probably increase with the order of sites because the tension of the leg increases with time. However, without further information about the elasticity and geometry of the leg, it is fruitless to pursue the model beyond its current stage.
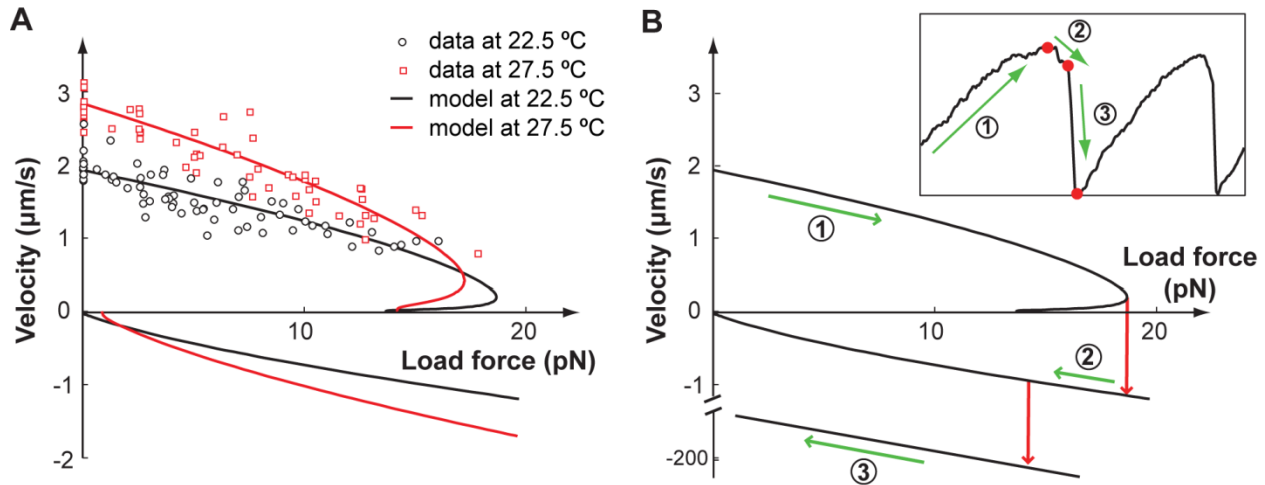
Figure 2-4: The load-velocity curve explains the dynamical behavior in the laser trap experiments. (**A**) Load force vs. velocity curve. The model results are computed beyond the velocity regime measured in the experiments. Hysteresis is predicted by the model. (**B**) Mapping of the dynamical trajectory onto the load-velocity curve. The middle branch of the load-velocity curve is unstable. The straight line added at the bottom of the plot shows the hydrodynamic load-velocity curve, i.e. when the cell is off the substrate. The dynamical trajectory measured from an optically trapped mycoplasma is shown in the inset (taken from (Miyata, Ryu et al. 2002)). The labeled green arrows along the load-velocity curve and the dynamic trajectory show in correspondence the 3 motility phases of the cell: (1) forward; (2) backward; (3) free after detachment. The red arrows on the load-velocity curve and the red dots on the trajectory indicate corresponding transitions between the 3 phases. This branching load-velocity curve explains the forward-to-backward transition in the dynamical trajectory. But the backward-to-break-off transition cannot be explained without further experimental information.

The hysteresis in the load-velocity curve explains the dynamical trajectory observed in the experiment, in which the mycoplasma is attached to an optically trapped bead. This experiment captures the slowing down of the motion to near-stall (fig.5 in (Miyata, Ryu et al. 2002); also shown in the inset of Figure 2-4B). At first, the cell drags the trapped bead away from the center of the laser beam, thus increasing the load force experienced (the laser trap is well approximated by a quadratic potential, i.e. a linear spring). The cell slows until it reaches the position in the trap that generates a load force ~20 pN. At this force, the cell begins to slide backwards, and

eventually breaks off from the substrate. Then the cell is quickly drawn back to the center of the trap where it reattaches, and the cycle repeats.

The corresponding trajectory is mapped out on the load-velocity curve, shown in Figure 2-4B. The cell first trace down the upper branch of the load-velocity curve until it reaches the nose. It cannot follow the unstable middle branch—otherwise it would have a positive velocity yet move in the backward direction with decreasing load force. Thus it must jump to the lower branch of the curve. On this branch the cell begins to slide back (negative velocity). However, this does not persist long before the cell detaches from the substrate. Now the cell is quickly drawn back to the center of the trap with a much larger velocity determined by its hydrodynamic drag.

2.3 Discussion

We have constructed a minimal mechanochemical model of the mycoplasma motility apparatus based on current knowledge. The model is able to explain the interesting biophysical properties of the motility, especially the steep, sub-Arrhenius dependence of velocity on temperature. The model assumes the simplest coupling between the motor, intermediate segment, and foot, and no coupling between legs. Each leg simply rows forward and backwards which, if completely symmetric, would not produce any net forward motion. Net forward motion is guaranteed by the asymmetric geometry of the leg, which causes the foot to release from the substrate more easily when peeled from the back. The high temperature sensitivity of the peel-off rate results from the multiplicity of the single-site Arrhenius factor. The factor decreases as temperature rises, contributing to the sub-Arrhenius behavior of the temperature-velocity curve. Furthermore, the weakly-facilitated foot release during the power stroke curtails the positive impulses and reduces the velocity at high temperatures. Finally, the dynamical process measured in laser trap experiments is explained qualitatively by the resultant load-velocity curve.

Certain biological parameters are estimated through the model. The binding and release rates of single binding site directly result from the fitting to the experimental data. They are all on the order of 10^3 hertz (Table 2-1). The peel-off rate is 2−3 times as large as the weakly-facilitated release rate. The average cycle period of the leg in the unloaded cell is on the order of $10-10^2$ ms, which shortens with increasing temperature (Figure 2-5A). The power stroke and the subsequent leg re-stretching each takes about 40% of the period in average (Figure 2-5B). Peeling off the foot takes about 15% of the period. For the rest of the cycle period the foot is unbound. Notice that the fraction of unbound time increases significantly with temperature, which helps explain that the cell easily detaches from the substrate at high temperatures. The cycle period also increases with increasing load force or decreasing velocity. When the cell approaches stall, the cycle is limited by the spontaneous release of the foot, and the cycle period tends to the reciprocal of that rate. The Stokes efficiency, estimated by $F_L V \tau / \Delta G_{ATP}$, is about 10% for the optimal load; here F_L is the load force and τ the cycle period. The above estimations fall in the proper biological range. Nevertheless they are very rough, limited by the coarse-graining of the model.

The model also provides several predictions for experimental comparison. For example, the cell velocity peaks at a certain sialic acid density on the substrate (Figure 2-6A). This was shown by experiments changing the concentration of sialic acid used for coating the substrate (c.f. fig.6 in

(Nagai and Miyata 2006)). Only qualitative comparison can be drawn at this moment because we lack detailed information about the mechanism of foot binding as well as the relationship between sialic acid concentration in the coating medium and the sialic acid density finally presented on the surface of the substrate. We can also predict the effect of medium viscosity on the load-velocity curve (Figure 2-6B). Increasing the viscosity reduces the velocities for any given load force. Also, the load-velocity appears more concave at higher medium viscosity. This change occurs because the resetting process is slowed at high viscosity and the hydrodynamic drag forces become more significant, compared with the other forces involved in the motility. Consequently, the cycle period is lengthened and the net force impulse provided per cycle affected as well (cf. Eqs.(2.32), (2.34), (2.37) and (2.38) in Appendix D).
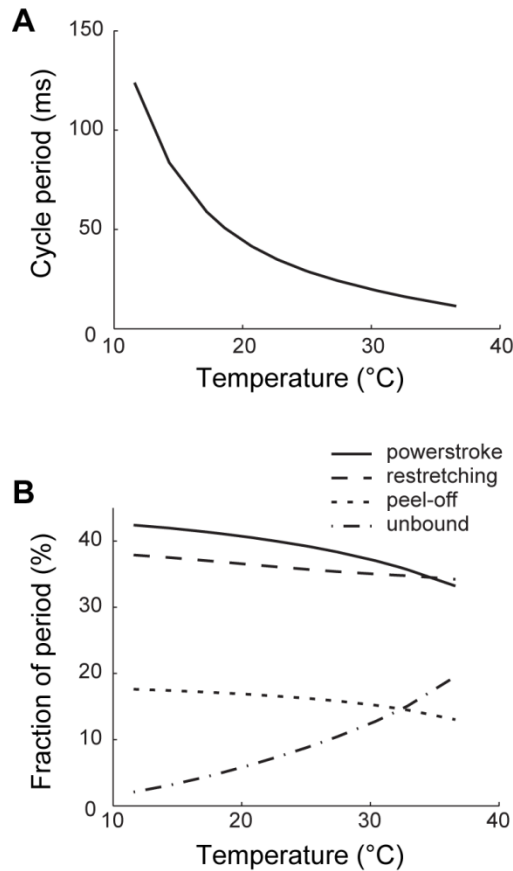
Figure 2-5: Cycle period and residence times of each stage change with temperature. (**A**) The cycle period decreases with temperature, ranging between $10-10^2$ ms in the relevant temperature range. (**B**) Temperature affects the durations of the power stroke (solid), re-stretching (dashed), peel-off (dotted) and the unbound states (dash-and-dotted). These results are computed from Eq.(2.32) in Appendix D.

19
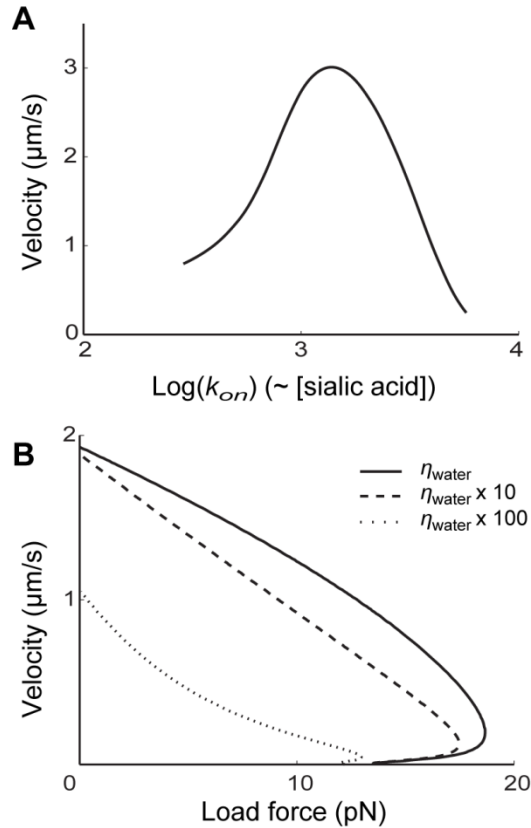
Figure 2-6: Predictions of the model. (**A**) The effect of sialic acid concentration on the cell velocity. The horizontal axis shows the logarithm of the single-site binding rate, which is directly related to the density of sialic acid on the substrate surface. The model predicts the existence of an optimal sialic acid density for mycoplasma motility, to be compared with the experiment result presented in fig.6 of (Nagai and Miyata 2006). (**B**) The effect of viscosity on the load-velocity curve. The curves are computed for the mediums bearing the normal water viscosity (solid line), 10 times larger (dashed line) and 100 times larger (dotted line). The cell velocity decreases when viscosity increases. And the load-velocity curve becomes more concaved with larger viscosity.

Single molecule experiments on single legs are probably the best way to test the foot-substrate interaction mechanism proposed here. According to our model, the leg should break off from the substrate much easier under forward pulling force than it does under backward pulling force. Further structural information on the binding sites would also be useful in narrowing down the range of model parameters and estimating the energy barrier involved in the unbinding process.

The model for mycoplasma motility can be generalized to other motility systems. Many "walking" molecular motors such as kinesin and myosin, show steep, sub-Arrhenius temperature-velocity curves (Anson 1992; Decuevas, Tao et al. 1992; Bohm, Stracke et al. 2000; Fenimore, Frauenfelder et al. 2002; Watanabe, Iino et al. 2008). Even in rotary motors, like the *E. coli* flagellar motor (Berg 2003; Kojima and Blair 2004), the way that the stators push on the

20

rotor is analogous to the mycoplasma legs walking on the substrate. Unlike the intuitive considerations of the catalytic biochemistry, we proposed the motor-substrate interaction as the major factor to explain the temperature sensitivity. This theory can be more easily tested with experiments on molecular motors because there are more techniques to manipulate them.

Limited by the information on mycoplasma motility, our model is quite coarse-grained with many approximations. The peel-off mechanism itself was derived with the approximation of identical off rates for all binding sites. A refined model with more realistic description of the rates can probably fit the stall force better. Moreover, the model is built on the horizontal spatial coordinate only. The vertical components of the forces, however, probably play a critical role in the peel-off of the foot, and even the break-off of the whole cell. Adding such details entail a more refined model. However, without knowing the detailed molecular mechanism of the foot-substrate interaction, such elaboration is merely guesswork.

Appendix A: Hidden coordinates for the motor

The molecular motor is a large protein, and so a complete atomic description of its motion requires a very high dimensional configuration space: at least 3N-dimensional, where N is the number of atoms. Generally, the large scale motions of proteins are dominated by a small number of "modes". For example, we have simplified the motion of the motor to the opening and closing of the proximal part of the leg protein. By doing so, we are essentially projecting the high-dimensional periodic motion onto one single coordinate and treating it as a 1-dimensional periodic oscillation. Although the resolved motor cycle appears to be moving forward and then backward along exactly the same trajectory, the "hidden" atomic degrees of freedom do not exactly retrace the same route. In particular, the second law of thermodynamics requires a loop in the force-displacement phase trajectory to account for the free energy consumption in the biochemical process. Such a loop is impossible when we simplify the motion to one dimension. We must include at least two configurational coordinate, say (z, θ), so as to form a cyclic loop in the (z, θ) plane. Therefore, the open conformation of the motor before the power stroke and the open conformation after the ADP release, although not distinguished in the model, are in general not equivalent. ATP can bind to the former conformation, but not the latter one. Rather than increasing the dimensionality of the model, we simply declare that ATP loading only happens after the leg fully resets to the front position. These issues are discussed more deeply in (Xing, Liao et al. 2005)

Appendix B: Derivation of peel-off rate of the foot

As proposed in the main text, the peel-off process of the foot can be represented by the following Markov chain:

$$Q \underset{k_{on}}{\overset{k_{off}}{\rightleftharpoons}} Q-1 \underset{k_{on}}{\overset{k_{off}}{\rightleftharpoons}} \cdots \underset{k_{on}}{\overset{k_{off}}{\rightleftharpoons}} 1 \underset{k_{on}}{\overset{k_{off}}{\rightleftharpoons}} 0 \text{ (all-off)}$$

The average peel-off rate equals the reciprocal of the mean first passage time (MFPT) to reach state 0 (all-off), starting from state Q (all-on). In the following derivation we use the probability transition matrix to calculate the vector of MFPT starting from each state. The first component of the vector gives the peel-off rate. Suppose the system stays at state i at the present time. In time dT, the system jumps to state j with probability $r_{ij} \cdot dT$ (figure below), where r_{ij} is the transition rate from state i to state j.

In the peel-off model discussed here, the transition rates are

$$r_{ij} = \begin{cases} k_{on} & \text{if } j = i+1 \\ k_{off} & \text{if } j = i-1 \\ 0 & \text{otherwise} \end{cases}$$

Now the MFPT from state j is T_j, so the MFPT from state i is dT plus the sum of all T_j, weighted by the transition probability from i to j in dT.

The above reasoning is expressed as

$$T_i = \sum_{j \neq i} T_j r_{ij} dT + (1 - \sum_{j \neq i} r_{ij} dT) T_i + dT, \quad i = 1,...,Q \tag{2.5}$$

Rearranging the above equation and canceling the common factor dT yields

$$\sum_{j \neq i} T_j r_{ij} - T_i \sum_{j \neq i} r_{ij} = -1 \tag{2.6}$$

Eq.(2.6) can be written in vector form as

$$\mathbf{P}^{\mathrm{T}}\mathbf{T} = \mathbf{-1} \tag{2.7}$$

where $\mathbf{T} = \{T_i\}_{i=0,...,Q}$ is the vector of MFPTs. Note that $T_0 \equiv 0$, since it takes no time to reach state 0 if the system starts from state 0. The operating matrix in Eq.(2.7) happens to be the transpose of the probability transition matrix of the Markov chain, $\mathbf{P}$.

$$\mathbf{P} = \begin{bmatrix} -k_{on} & k_{off} & & & & & & \\ k_{on} & -k_{on}-k_{off} & k_{off} & & & & & \\ & k_{on} & -k_{on}-k_{off} & & & & & \\ & & k_{on} & & \ddots & & & \\ & & & & \ddots & & & \\ & & & \ddots & & k_{off} & & \\ & & & & -k_{on}-k_{off} & k_{off} & \\ & & & & k_{on} & -k_{off} \end{bmatrix} \tag{2.8}$$

$\mathbf{P}$ is singular because all columns sum to zero. But $T_0 \equiv 0$ eliminates one unknown. Eq.(2.7) is solvable when the first column and the first row of $\mathbf{P}$ are removed and vector $\mathbf{T}$ is shortened by the first element. The solution to Eq.(2.7) gives the MFPT from state Q to state 0. Its reciprocal, the peel-off rate, is given in Eq.(2.2) in the main text.

Solving Eq.(2.6) (i.e. Eq.(2.7) with the T_0 dimension removed) is shown in the following. There are altogether Q equations and Q unknowns:

$$k_{off}T_{i-1} + k_{on}T_{i+1} - (k_{on} + k_{off})T_i = -1, \ i = 1,...,Q-1 \tag{2.9}$$

$$k_{off}T_{Q-1} - k_{off}T_Q = -1 \tag{2.10}$$

Now let $\Delta T_i := T_{i+1} - T_i$, then Eq.(2.9) and Eq.(2.10) can be transformed into

$$k_{on}\Delta T_i - k_{off}\Delta T_{i-1} = -1, \ i = 1,...,Q-1 \tag{2.11}$$

$$-k_{off}\Delta T_{Q-1} = -1 \Rightarrow \Delta T_{Q-1} = 1/k_{off} \tag{2.12}$$

Let $\Delta T_i' := \Delta T_i - \dfrac{1}{k_{off} - k_{on}}$, then Eq.(2.11) and Eq.(2.12) are equivalent to

$$\Delta T_{i-1}' = K\Delta T_i' \tag{2.13}$$

$$\Delta T_{Q-1}' = -\dfrac{K}{k_{off} - k_{on}} \tag{2.14}$$

where $K = k_{on}/k_{off}$.

Eq.(2.13) and Eq.(2.14) give

$$\Delta T_i' = K^{Q-i-1}\Delta T_{Q-1}' = -\dfrac{K^{Q-i}}{k_{off} - k_{on}} \tag{2.15}$$

Thus,

$$\begin{aligned}
T_Q &= T_0 + \sum_{i=0}^{Q-1} \Delta T_i \\
&= \sum_{i=0}^{Q-1}\left(\Delta T_i' + \dfrac{1}{k_{off} - k_{on}} \right) \\
&= \dfrac{\sum_{i=0}^{Q-1}\left(1 - K^{Q-i}\right)}{k_{off} - k_{on}} \\
&= \dfrac{1}{k_{off}(1-K)}\left(Q+1 - \dfrac{1-K^{Q+1}}{1-K} \right) \\
&= \dfrac{1}{k_{off}} \dfrac{Q-(Q+1)K + K^{Q+1}}{(1-K)^2}
\end{aligned}$$

The reciprocal of the above gives the peel-off rate R_p:

$$R = k_{off}\dfrac{(1-K)^2}{Q-(Q+1)K + K^{Q+1}} \tag{2.16}$$

24

Appendix C: Derivation of weakly-facilitated and spontaneous release rates of the foot

$$Q \underset{k_{on}'}{\overset{Qk_{off}'}{\rightleftarrows}} Q-1 \underset{2k_{on}'}{\overset{(Q-1)k_{off}'}{\rightleftarrows}} \cdots \underset{(Q-1)k_{on}'}{\overset{2k_{off}'}{\rightleftarrows}} 1 \underset{Qk_{on}'}{\overset{k_{off}'}{\rightleftarrows}} 0 \text{ (all-off)}$$

A Markov chain model similar to the one described above gives the weakly-facilitated release rate and the spontaneous release rate of the foot. In this model, we also have $Q+1$ states connected in a queue. But the transition rates between each pair of neighboring states change slightly, because the on/off event does not have to happen in a strictly sequential fashion. At state Q, any of the $Q\text{-}i$ unbound sites can bind, and any of the i bound sites can unbind. The transition rates become

$$\begin{aligned} r_{i-1 \to i} &= (Q-i+1) \cdot k_{on} \\ r_{i \to i-1} &= i \cdot k_{off} \end{aligned} \tag{2.17}$$

and the transition matrix is

$$\mathbf{P} = \begin{bmatrix} -Qk_{on} & k_{off} & & & & & & \\ Qk_{on} & -(Q-1)k_{on}-k_{off} & 2k_{off} & & & & & \\ & (Q-1)k_{on} & -(Q-2)k_{on}-2k_{off} & & & & & \\ & & (Q-2)k_{on} & \ddots & & & & \\ & & & & \ddots & & & \\ & & & & \ddots & (Q-1)k_{off} & & \\ & & & & & -k_{on}-(Q-1)k_{off} & Qk_{off} \\ & & & & & k_{on} & -Qk_{off} \end{bmatrix} \tag{2.18}$$

Because the foot can start from any state with corresponding residence probability, the reciprocal of the whole-foot rate is the weighted average MFPT. Solving Eq.(2.18) with similar procedures given in Section I gives Eq.(2.4) in the main text.

The following is a simpler derivation of the same result. For each binding site the mean residence times of the unbound and the bound state are, $\tau_u = 1/k_{on}$, $\tau_b = 1/k_{off}$, respectively. The probability of finding a site in the unbound state is

$$p_u = \frac{\tau_u}{\tau_b + \tau_u} \tag{2.19}$$

Suppose the Q states of the foot are categorized into two: the all-detached state $\{0\}$, and the compound state with at least one bound site $\{1,2,\ldots,Q\}$. The two newly defined states of the foot obey the same law as Eq.(2.19). The probability of the all-detached state is p_u^Q, as computed in Eq.(2.19). Let T_{off} be the mean residence time of the all-detached state, and T_{on} that of the compound state. Then we have

$$\frac{T_{off}}{T_{on}+T_{off}} = p_u^Q = \left(\frac{\tau_u}{\tau_b+\tau_u}\right)^Q \tag{2.20}$$

T_{off} is the reciprocal of the rate of having any one of the Q sites bind to the substrate, which is Q times k_{on}. Substituting $T_{off} = 1/Qk_{on} = \tau_u/Q$ into Eq.(2.20) yields

$$T_{on} = \frac{\tau_u}{S}\left[\left(1+\frac{\tau_b}{\tau_u}\right)^Q -1\right] \tag{2.21}$$

Then the reciprocal of T_{on} is the foot unbinding rate, same as Eq.(2.4) in the main text.

$$R = \frac{Q/\tau_u}{\left(1+\tau_b/\tau_u\right)^Q -1} = \frac{Qk_{on}}{\left(1+k_{on}/k_{off}\right)^Q -1} \tag{2.22}$$

Appendix D: Derivation of the load-velocity curve

The following derivation takes into account of the weakly-facilitated foot release during the power stroke and the spontaneous foot release during the re-stretching. The resultant load-velocity curve was shown in Figure 2-4A in the main text. Additional parameters and their values are listed in Table 2-2.

Consider the ensemble of feet which bind and unbind with the substrate (top left panel of Figure 2-7). Each foot is characterized by one continuous state variable, its displacement, x, relative to the beginning of a power stroke, as seen in the cell's frame of reference. The important "checkpoints" are $x = 0$ (beginning of power stroke), $x = \lambda$ (end of power stroke) and $x = \lambda+L$ (unstressed backward position). When a foot completes a power stroke crossing from $x < \lambda$ to $x > \lambda$, we assume that the motor hydrolyzes ATP, and is set to the "open" configuration.

In addition, we have three discrete states of the foot, one bound state and two unbound (thick horizontal bars, top left panel of Figure 2-7). The bound feet are stuck to the substrate, and in the cell's frame of reference, translate at the gliding velocity V. The ensemble density of bound feet is denoted $\rho_0(x)$, in $x \geq 0$. It is convenient to distinguish two states of unbound feet. Feet of the first state has unbounded during the power stroke ($0 < x < \lambda$). They are rapidly pulled to $x = \lambda$ at velocity f_m/ζ_f, where f_m is the motor force, and ζ_f the hydrodynamic drag coefficient of the foot. The ensemble density of these feet is denoted $\rho_1(x)$, in $0 \leq x \leq \lambda$. The second unbound state accounts for the returning feet heading back to $x = 0$ at velocity $-f_r/\zeta_f$. Here, $-f_r$ is the weak restoring force that drives the kinking of the leg and returning of the feet. The density of the returning feet is denoted $\rho_2(x)$, in $x \geq 0$.
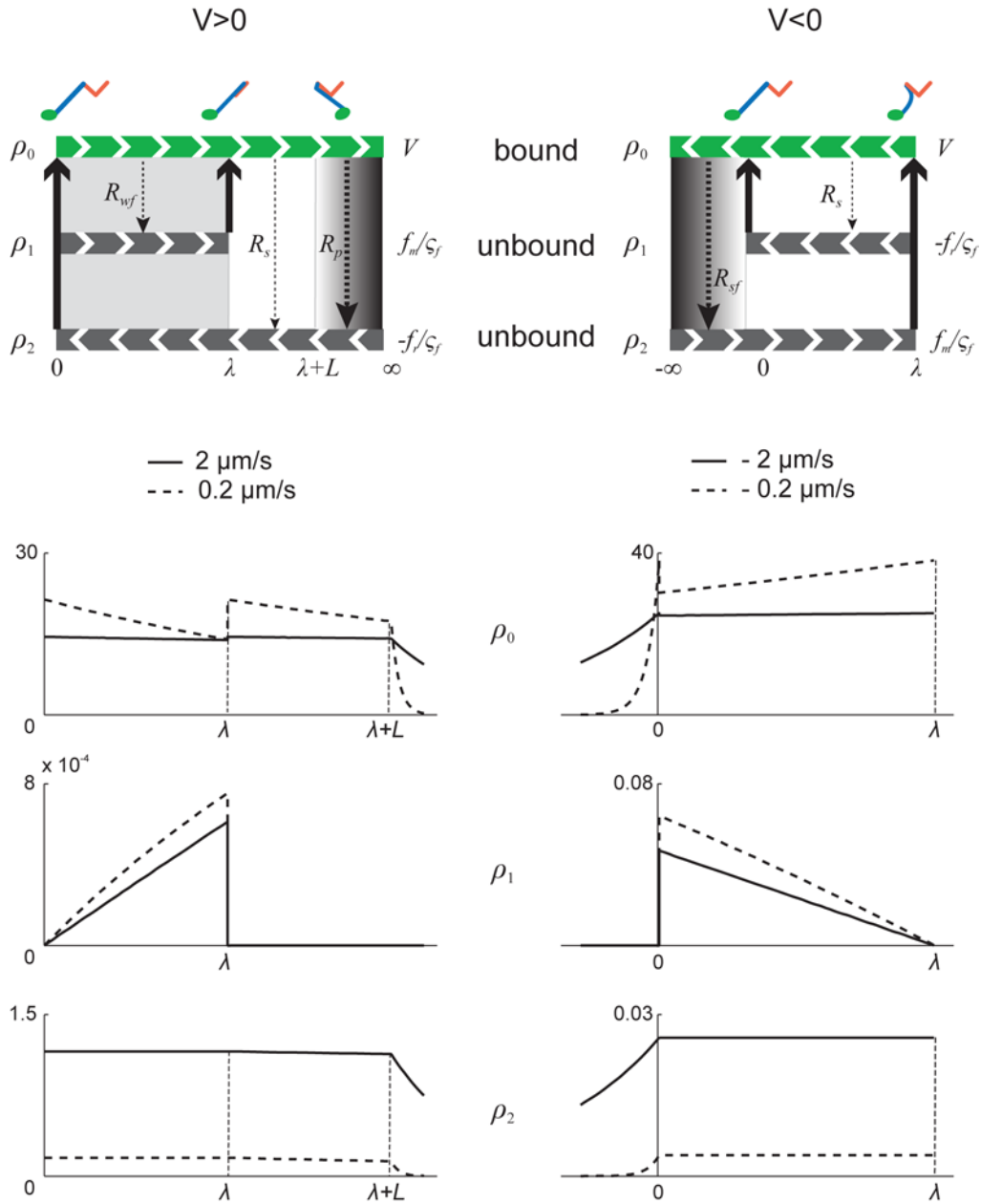
V>0   V<0

ρ₀ ... V   bound   ρ₀ ... V

R_{wf} R_s R_p f_m/ς_f unbound   ρ₁ ... R_s ... $-f/\varsigma_f$

ρ₁ R_s R_p f_m/ς_f unbound R_{sf}

ρ₂   0   λ   λ+L   ∞ $-f/\varsigma_f$ unbound   ρ₂   -∞   0   λ f_m/ς_f

— 2 µm/s
--- 0.2 µm/s

— - 2 µm/s
--- - 0.2 µm/s

30

0   λ   λ+L   ρ₀

40

0   λ   ρ₀

8 × 10⁻⁴

0   λ   ρ₁

0.08

0   λ   ρ₁

1.5

0   λ   λ+L   ρ₂

0.03

0   λ   ρ₂

Figure 2-7: Illustration of the transport equations and the resultant density distribution of the feet. The cartoons on the top illustrate Eqs.(2.23)-(2.30) and Eqs.(2.35). Left: V > 0. The horizontal bars show the three different states of the foot, bound (ρ_0), released during the power stroke with weak facilitation (ρ_1), and spontaneously released or peeled off after the power stroke (ρ_2). Corresponding foot conformations are labeled on the very top. The directions of foot transport in these states are shown with white arrows in the bar and velocities labeled on the right end, both in the frame of reference of the cell body. The thick solid arrows pointing upward illustrate the rebinding of the free foot. The dashed arrows pointing downward show different ways that the foot can release from the substrate, their thickness indicating the relative

27

magnitude of the rates. The shadings illustrate the forces acting on the foot: motor force during the power stroke (*light even shade*) and peel force after stretched (*monotonically darker shade*). Right: V < 0. All labels bear similar meanings. There are also three different states of the foot, bound (ρ_0), spontaneously released during the post-power-stroke relaxation (ρ_1), and snatched off during the power stroke (ρ_2). The diagrams below the cartoons show examples of typical density distribution of the feet at different states at 22.5°C.

Now we write the steady state (time independent) transport equations for $\rho_0(x)$, $\rho_1(x)$ and $\rho_2(x)$. $\rho_0(x)$ satisfies the ODE:

$$V\frac{d\rho_0}{dx} = -R(x)\rho_0 \tag{2.23}$$

The LHS of Eq.(2.23) is the convective derivative (time derivative of $\rho_0(x(t))$, at $x(t)$ with $\dot{x} = V$). $R(x)$ is the rate coefficient for foot unbinding. We expect a piecewise character in $R(x)$ as illustrated in Figure 2-8:

$$R(x) = \begin{cases} R_{wf}(x), & 0 \le x < \lambda \\ R_s(x), & \lambda \le x < \lambda + L \\ R_p(x), & x \ge \lambda + L \end{cases} \tag{2.24}$$

Here, R_{wf} denotes the weakly facilitated release during the power stroke, R_s the spontaneous release rate and R_p the peel-off rate. According to the amount of force acting on the foot in each case, the relative magnitude of the three rates should be $R_p > R_{wf} > R_s$.
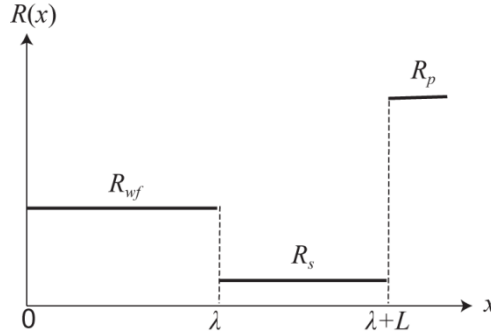

Figure 2-8: Piecewise function of $R(x)$.

The transport ODE for $\rho_1(x)$ in $0 \le x \le \lambda$ is based on translational velocity $\dot{x} = f_m/\zeta_f$, and the source due to foot release in $0 < x < \lambda$.

$$\frac{f_m}{\zeta_f}\frac{d\rho_1}{dx} = R(x)\rho_0, 0 \le x \le \lambda \tag{2.25}$$

Since all feet at the beginning of the power stroke are assumed to be bound, we have the boundary condition:

$$\rho_1(0) = 0 \tag{2.26}$$

The transport equation for $\rho_2(x)$, the returning foot, is based on the translational velocity $\dot{x} = -f_r/\zeta_f$ and the sources indicating the spontaneous foot release and the peel-off:

$$-\frac{f_r}{\zeta_f}\frac{d\rho_2}{dx} = \begin{cases} 0, & 0 \le x < \lambda \\ R(x)\rho_0, & x \ge \lambda \end{cases} \tag{2.27}$$

Finally, we have two flux balance boundary conditions:

$$V\rho_0(0) = \frac{f_r}{\zeta_f}\rho_2(0) \tag{2.28}$$

$$V\left(\rho_0(\lambda^+) - \rho_0(\lambda^-)\right) = \frac{f_m}{\zeta_f}\rho_1(\lambda) \tag{2.29}$$

The LHS of Eq.(2.28) is the flux of the unbound feet returning to $x = 0$, and the RHS the flux of feet starting the power stroke. The balance holds upon the assumption that the power stroke starts as soon as a foot returns to $x = 0$. Eq.(2.29) represents the jump of foot density at $x = \lambda$ contributed by the rebinding of the foot that have unbound during the power stroke. This equation holds when we assume that the rebinding happens very fast compared to the time scales resolved in these equations.

Eqs.(2.23)-(2.29) determines $\rho_0(x)$, $\rho_1(x)$ and $\rho_2(x)$ up to a multiplicative constant. This constant can be determined by normalization:

$$\int_0^\infty \rho_0(x)dx + \int_0^\lambda \rho_1(x)dx + \int_0^\infty \rho_2(x)dx = 1 \tag{2.30}$$

Assume all foot release rates are invariant with position. Then Eqs.(2.23)-(2.30) can be solved analytically with solutions:

$$TV \cdot \rho_0(x) = \begin{cases} \exp\left(-\dfrac{R_{wf}\,x}{V}\right), & 0 \le x < \lambda \\[2mm] \exp\left(-\dfrac{R_s(x-\lambda)}{V}\right), & \lambda \le x < \lambda + L \\[2mm] \exp\left(-\dfrac{R_s L + R_p(x-\lambda-L)}{V}\right), & x \ge \lambda + L \end{cases}$$

$$TV \cdot \rho_1(x) = \frac{\varsigma_f V}{f_m}\left(1 - \exp\left(-\frac{R_{wf}\,x}{V}\right)\right), \qquad 0 \le x \le \lambda$$

$$TV \cdot \rho_2(x) = \begin{cases} \dfrac{\varsigma_f V}{f_r}, & 0 \le x < \lambda \\[2mm] \dfrac{\varsigma_f V}{f_r}\exp\left(-\dfrac{R_s(x-\lambda)}{V}\right), & \lambda \le x < \lambda + L \\[2mm] \dfrac{\varsigma_f V}{f_r}\exp\left(-\dfrac{R_s L + R_p(x-\lambda-L)}{V}\right), & x \ge \lambda + L \end{cases}$$

(2.31)

where T is the average duration of the whole cycle.

$$T = \frac{1-\exp\left(-R_{wf}\lambda/V\right)}{R_{wf}} + \frac{1-\exp\left(-R_s L/V\right)}{R_s} + \frac{\exp\left(-R_s L/V\right)}{R_p}$$
$$+ \frac{\varsigma_f}{f_m}\left(\lambda - V\frac{1-\exp\left(-R_{wf}\lambda/V\right)}{R_{wf}}\right)$$
$$+ \frac{\varsigma_f}{f_r}\left(\lambda + V\frac{1-\exp\left(-R_s L/V\right)}{R_s} + V\frac{\exp\left(-R_s L/V\right)}{R_p}\right)$$

(2.32)

The first three terms in Eq.(2.32) correspond to the average time the bound foot spends during the power stroke, re-stretching and peel-off respectively. The 4th term represents the time it takes for the free foot to reach the post-power-stroke position after its weakly facilitated release from the substrate. The last term represents the time that the free foot resets to the front position after either the spontaneous release or the peel-off. The load-velocity relation is calculated with the force balance equation. The load force is balanced by the net force contributed by all feet. The bound feet provide positive force during the power stroke, negative force during the peel-off process, and the weak resetting force during the re-stretching. The free foot in state 1 is dragged in the medium with the motor force; and the free foot in state 2 is dragged with the resetting force. Therefore, the force balance equation reads

$$\left(F_L + \varsigma_b V\right)/N = f_m\int_0^\lambda \rho_0(x)dx - f_r\int_\lambda^{\lambda+L}\rho_0(x)dx - \int_{\lambda+L}^\infty \kappa(x-\lambda-L)\rho_0(x)dx$$
$$+ f_m\int_0^\lambda \rho_1(x)dx - f_r\int_0^\infty \rho_2(x)dx$$

(2.33)

Plugging in Eq.(2.31) gives

$$F_L = -\zeta_b V$$

$$+ \frac{N}{T} \left\{ \frac{f_m - \zeta_f V}{R_{wf}} \left(1 - \exp\left(-\frac{R_{wf}\lambda}{V} \right) \right) - \frac{\left(\kappa/R_p - \zeta_f \right)V}{R_p} \exp\left(-\frac{R_s L}{V} \right) + \frac{f_r - \zeta_f V}{R_s} \left(1 - \exp\left(-\frac{R_s L}{V} \right) \right) \right\}$$

(2.34)

The impulse balance equations given in the main text (Eq.(2.1) and Eq.(2.3)) are simplified version of Eq.(2.34). Eq.(2.3) corresponds to the case where ζ_f, ζ_b, R_s, $f_r \rightarrow 0$. These assumptions have been elaborated in the main text before the introduction of the impulse balance equations. Eq. (2.1) is the further simplification when $R_{wf} \ll V/\lambda$.

The derivation of the $V < 0$ case is similar, as illustrated by the top right panels of Figure 2-7. There are again three states of the foot, albeit with different meanings for the states of the free foot. This is because the leg cycle in the negative regime is asymmetric to that in the positive regime. The major break-off of the foot from the substrate occurs during the power stroke when the leg is overstretched. Since the force is exerted in the opposite direction of the tip of the foot, it does not create a peel effect. The break-off process is similar to the weakly-facilitated and spontaneous release, only with much stronger force facilitation. Therefore, we labeled the new rate as R_{sf} to stand for "strongly-facilitated". The leg will be over-relaxed after the motor releases ADP and opens up. It re-stretches while the foot moves on towards the starting position for the next power stroke. During the re-stretching the foot can also spontaneously release from the substrate with essentially the same rate used in the case $V > 0$. Now ρ_1 represents the density of the foot that has been spontaneously released during re-stretching. ρ_2 corresponds to the foot that has been snatched off the substrate during the power stroke. The governing transport ODEs are given in Eqs.(2.35).

$$\begin{cases} V\dfrac{d\rho_0}{dx} = -R(x)\rho_0, & \text{(a)} \\[2mm] -\dfrac{f_r}{\zeta_f}\dfrac{d\rho_1}{dx} = R(x)\rho_0, & 0 < x \leq \lambda & \text{(b)} \\[2mm] \dfrac{f_m}{\zeta_f}\dfrac{d\rho_2}{dx} = \begin{cases} R(x)\rho_0, & x \leq 0 \\ 0, & 0 < x \leq \lambda \end{cases} & \text{(c)} \\[4mm] -V\rho_0(\lambda) = \dfrac{f_m}{\zeta_f}\rho_2(\lambda), & \text{(d)} \\[2mm] -V\left(\rho_0(0^-) - \rho_0(0^+)\right) = \dfrac{f_r}{\zeta_f}\rho_1(0), & \text{(e)} \\[2mm] \rho_1(\lambda) = 0, & \text{(f)} \\[2mm] \displaystyle\int_{-\infty}^{\lambda}\rho_0 dx + \int_0^{\lambda}\rho_1 dx + \int_{-\infty}^{\lambda}\rho_2 dx = 1, & \text{(g)} \end{cases}$$

(2.35)

with the piecewise foot release rate

$$R(x) = \begin{cases} R_{sf}(x), & x \le 0 \\ R_s(x), & 0 < x \le \lambda \end{cases} \tag{2.36}$$

The meanings of each equation above are similar to those for positive velocities. The resulting load force as a function of velocity is

$$F_L = -\zeta_b V + \frac{N}{T}\left\{ \frac{f_m - \zeta_f V}{R_{sf}} - \frac{\kappa V}{R_{sf}^2} - \frac{f_r + \zeta_f V}{R_s}\left(1 - \exp\left(\frac{R_s \lambda}{V}\right)\right) \right\} \tag{2.37}$$

where the average cycle duration is

$$T = \frac{1}{R_{sf}} + \frac{1 - \exp(R_s\lambda/V)}{R_s} + \frac{\zeta_f}{f_m}\left(\lambda - \frac{V}{R_{sf}}\right) + \frac{\zeta_f}{f_r}\left(\lambda + V\frac{1 - \exp(R_s\lambda/V)}{R_s}\right) \tag{2.38}$$

Similar to Eq.(2.32), the first two terms in Eq.(2.38) correspond to the average time the foot spends during the power stroke and the re-stretching. The other two represent the average resetting time after the foot releases from the over-stretched position and the unstretched position. The duty ratio equals the sum of the first two terms divided by the cycle period.

Typical foot density distributions of each state in the $V > 0$ and $V < 0$ cases are shown in Figure 2-7. ρ_0 dominates over ρ_1 and ρ_2 in magnitude in both $V > 0$ and $V < 0$ cases because the unbound foot translocates very fast with a small hydrodynamic drag coefficient, leading to a small residence time. Furthermore, the magnitude of the density of each unbound state is determined by the corresponding driving force during the state and the foot release rate. For example, ρ_1 at $V > 0$ is extremely small because the foot is released with the weakly facilitated rate R_{wf}, and then driven fast by the relatively large force f_m. By contrast, ρ_2 at $V > 0$ is much larger because the majority of the foot is released by the much larger peel-off rate R_p, and then driven by the much smaller restoring force f_r.

Table 2-2: List of additional parameters used for the load-velocity curve.

Parameters	Values	Physical meaning
L	25 nm	distance between the end of power stroke and backward re-stressed position
f_r	0.005 pN	weak resetting force
ζ_f	200 pN·s/m	hydrodynamic drag coefficient of the foot
ζ_b	2×10^4 pN·s/m	hydrodynamic drag coefficient of the cell body
k''_{off}	1.7×10^3 s^{-1} (16.8 k_BT)	spontaneous release rate of single site (and its Arrhenius factor)

Chapter 3   Myxobacteria A-Motility

The bacterial cytoskeleton determines cell shape and mediates cell division. Recent discoveries on myxobacteria motility reveal the first known prokaryotic example of a cytoskeleton driven cell motility. During cell locomotion, a double helical MreB structure rotates in the cell's cytoplasm. The driving motors are homologous to the MotA-MotB stator that drives the rotation of the bacterial flagellar motor. These observations suggest an entirely new model for bacterial motility in which motors driven by ion motive force move along the helical cytoskeleton to generate propulsive forces. This mechanism may be widespread in bacteria, since both MreB homologs and MotA-MotB homologs are common across a variety of bacterial species, including many that move in the absence of flagella.

We have constructed a biophysical model for this motility mechanism. Within the general framework of motors running on a double helical track, the model introduces cargo-mediated force generation as a key assumption. The two types of cargo, causing high drag and low drag respectively, are unequally distributed along the two helical strands, thereby generating a net propulsive force. The unequal distribution results from unequal cargo exchange rates at the poles. Besides reproducing the cell velocity and the rotational velocity of the track, our model also explains many intriguing observations in myxobacteria motility, including periodic reversals of cells, short pauses before cell reversal and a series of experiments showing the dynamics of motility-related protein clusters at the cell poles and along the substrate interface.

3.1 Introduction

The myxobacterium *Myxococcus xanthus* is a soil-dwelling bacterium with a complex life cycle staged as vegetative swarming, predation, fruiting body and myxospores formation. These complicated social behaviors require large scale coordinated movements of the cells (Kaiser 2003; Mignot 2007; Zusman, Scott et al. 2007; Mignot and R. Kirby 2008; Mauriello, Mignot et al. 2010). *M. xanthus* is rod-shaped and 5−10 µm in length. Under lab condition, the cells move on agar at about 2−4 µm/min and reverse direction every 7 minutes or so (Zusman, Scott et al. 2007; Mauriello, Mignot et al. 2010). The cells can only move on solid substrates and become non-motile on liquid surfaces (Zusman, Scott et al. 2007). The motility is driven by two sets of apparatus: the Social (S) motility engine and the Adventurous (A) motility engine. The S-engine sends out type IV pili from the cell's leading pole. The pili stick to the substrate or to neighboring cells, and then retract to pull the cell. The mechanism for the A-engine, however, remains unclear. Wolgemuth et. al. used a computational model to show the theoretical validity of an old proposal by Jahn (Jahn 1924; Wolgemuth, Hoiczyk et al. 2002) that A-motility is powered by extrusion and hydration of slime excreted from the cell's trailing pole. This mechanism, unfortunately, is disproven by recent observations that the A-engine is distributed along the cell rather than concentrated at the poles (Sliusarenko, Zusman et al. 2007).

A recent series of experiments by Mignot, Zusman *et. al.* revealed a surprising internal mechanism that accounts for the A-motility of *M. xanthus* (Mauriello and Zusman 2007; Mignot 2007; Mignot, Shaevitz et al. 2007; Mauriello, Nan et al. 2009; Mauriello, Mignot et al. 2010; Mauriello, Mouhamar et al. 2010). It involves proton-driven motors homologous to the bacterial

flagellar motor, as well as helical cytoskeleton filaments, which appear to be polymerized MreB (Mauriello, Mouhamar et al. 2010). Bacteria were previously thought to lack cytoskeleton until the discovery of actin-like MreB filaments, and microtubule-like FtsZ filaments. Then they were mainly believed to control cell shape and cell division (Adams and Errington 2009; Bramkamp and van Baarle 2009; Graumann 2009; Margolin 2009). Yet linear motors like myosin and kinesin that run along these cytoskeletons have never been found in bacteria. The A-engine of *M. xanthus* gives the first known prokaryotic example of such motility system.

Flagellar motor like proteins are involved in the A-engine of *M. xanthus*. The cell stops moving when treated with drugs like CCCP and nigericin, which disrupt the proton motive force (Sun, Wartel et al. 2010). The *M. xanthus* genome contains several pairs of homolog genes to the *E. coli motA* and *motB* genes (Nan, Mauriello et al. 2010). The transmembrane $MotA_4MotB_2$ complex acts as stator and proton channel in the *E. coli* flagellar motor. The complex changes conformation when the proton hops onto the transmembrane helix of MotB. The conformational change exerts a driving force on the rotor (Blair 2003). We shall assume that the motors in *M. xanthus* use a similar mechanism to push on the track.

In the A-engine of *M. xanthus*, the circular rotor track is replaced by a double helical filamentous structure. The helical geometry was first suggested by the equi-distant clustering of AglZ, an A-motility related protein (AMRP), along the cell-substrate interface (Mignot, Shaevitz et al. 2007). These clusters are almost stationary relative to the substrate. Recently, fluorescent imagining experiments (Nan and Zusman, in preparation) on AgmU, another AMRP, revealed a rotating double helical structure as the cell moves. The helix has a pitch similar to the double helical MreB filaments found in the cell (Mauriello, Mouhamar et al. 2010). Similar double helical MreB filaments have also been found in *E. coli* (Kruse, Moller-Jensen et al. 2003; Shih, Le et al. 2003) and *B. subtilis* (Jones, Carballido-López et al. 2001). Furthermore, A-motility stops when the cell is treated with A22, an MreB disintegrator (Mauriello, Mouhamar et al. 2010). Therefore, MreB is the most likely candidate for the track of the proton-driven motors.

Many AMRPs tend to concentrate at one cell pole, and periodically switch their pole concentrations as the cell reverses. For example, AglZ, AgmU and FrzS preferentially concentrate at the leading pole (Mignot, Merlie et al. 2005; Mignot, Merlie et al. 2007; Mignot, Shaevitz et al. 2007; Nan, Mauriello et al. 2010). After each cell reversal, the high concentration of these proteins shifts to the new leading pole. There are also other AMRPs that preferentially concentrate at the trailing pole, e.g. RomR (Leonardy, Freymark et al. 2007). The concentration shift occurs in ~40 seconds (Mignot, Merlie et al. 2005; Mignot, Shaevitz et al. 2007; Sun, Wartel et al. 2010), during which the proteins disperse along the cell. The time scale for diffusion along a cell 10 μm long matches the measured 40 seconds (estimated using the measured diffusion coefficient, 2.5 μm^2/s, of the maltose binding protein in the *E. coli* cytoplasm (Elowitz, Surette et al. 1999)). Therefore the change of AMRP concentrations is possibly mediated by diffusion.

Here we propose a mechanochemical model that explains the myxobacteria A-motility, the rotation of the track, the periodic reversal of the cell motion, and the dynamics of AMRP clusters.

3.2 Model and results

Our model features a mechanical system consisting of motors running along a double helical track, and anti-phased biochemical oscillators at the cell poles. The mechanical system drives the translocation of the cell and the rotation of the track. The biochemical oscillators control the reversal of the mechanical system.

Mechanics of A-motility

The A-engine of myxobacteria is simplified as transmembrane motor particles moving along a double helical track, exerting forces on it (Figure 3-1A). Equal and opposite forces are exerted on the cell membrane, cell wall and substrate. We assume that all the motors run in the same direction along the track. Due to the looped topology of the track the motors run in opposite directions relative to the substrate when they are on the opposite strands of the double helix. We distinguish between the two half-loops by referring to them as "left" and "right", corresponding to the direction of cell motion in Figure 3-1A.

For low Reynolds number motility asymmetry is necessary for net motion (Purcell 1977). The model cell cannot move if the left-bound motors and the right-bound ones contribute equal forces. The symmetry breaks when the numbers of left-bound and right-bound motors are different and/or when they exert different forces. The unequal number of motors alone cannot explain certain observations on the AMRP distributions. The reasons will be given in the discussion section after we elaborate on the mechanism of AMRP dynamics. In the following we introduce the mechanism for unequal motor forces.

A motor can exert different forces by carrying high-drag or low-drag cargo (Figure 3-1B, red for high-drag, blue for low-drag). The cargo consists of AMRPs. As the name suggests, the high-drag cargo causes larger drag force between the motor and the substrate, and the low drag cargo causes smaller force. In Figure 3-1B, we suggest a geometric factor underlying such difference in the drag. The bulky shape of the high-drag (red) cargo creates a bump at the surface of the cell envelope. As the motor carries the high-drag cargo through the substrate interface, the bump encounters a large drag force from the viscous slime between the cell and the substrate, so that the motors that engage the slime constitute the major force generating units in the system. As these high-drag motors are slowed down by the high drag at the substrate interface, they form clusters. Alternatively, the large drag could result from the formation of focal adhesion complexes, as suggested by Mignot (Mignot 2007; Mignot, Shaevitz et al. 2007; Mignot and R. Kirby 2008). This mechanism, however, requires penetration of the peptidoglycan layer by the cargo molecule. Consequently, the peptidoglycan has to be constantly lysed to allow relative motion between the cell and the substrate; this could render the cell wall unstable. Besides, the A-motility selectively prefers firm, dry substrate surface, e.g. 1.5% agar, than a soft, wet surface, e.g. 0.3% agar (Mauriello, Mignot et al. 2010). The AMRP clusters along the cell-substrate interface also appear brighter on firm surfaces—in the extreme case, directly on a glass surface (Nan, Mauriello et al. 2010). It is hard to explain the correlation between substrate firmness and A-motility by chemical (e.g. hydrogen) bonds required for focal adhesions. But bumps evidently encounter larger drag on dryer, firmer surfaces, resulting in stronger AMRP clustering. Therefore, the bump-on-the-surface mechanism is more plausible based on current knowledge about the A-

motility. Nevertheless, the model can be easily adapted to the focal adhesion scenario by greatly increasing the drag coefficient of the bump.
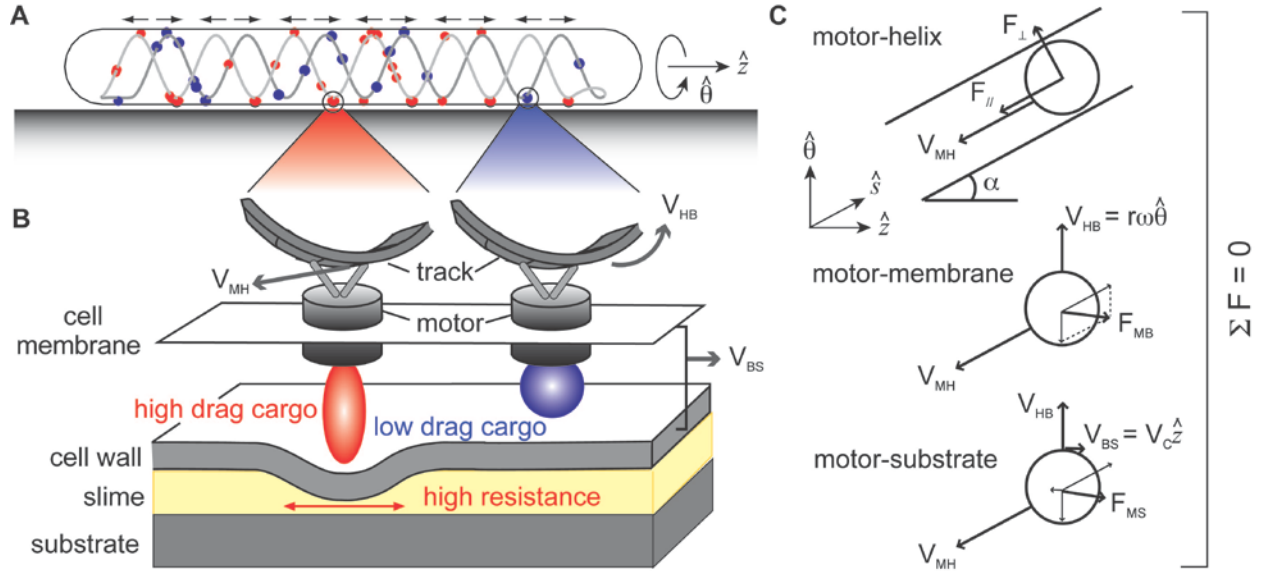

Figure 3-1: Setup of the mechanical model. (**A**) The motors run along the double helical track in the same direction. Relative to the substrate, the motors on the opposite strand run in opposite directions (*black arrows above the cell*). Blue dots: motors carrying low-drag cargo; red dots: motors carrying high-drag cargo; grey line: double helical track. $\hat{z}$ and $\hat{\theta}$ are unit vectors in the axial and rotational directions respectively. (**B**) Zoom-in view of the two types of motor-cargo complex. Here we assume the high drag on the red cargo results from its bulky geometry, which deforms the cell envelope locally. The bump formed at the surface causes high drag force as the motor tries to carry the cargo through the substrate interface. The relative velocities between various parts are indicated by grey arrows. The cell membrane and cell wall are assumed to have no relative motion. Subscript abbreviations: M = motor, H = helix, B = membrane/ wall, S = substrate, C = cell. (**C**) Force balance on the motor, projected onto the substrate surface. F: forces, V: velocities. The velocities in (B) are projected onto the substrate surface. The force between the motor (*circle*) and the helix (*area between two parallel lines*) along the helical direction, $F_{//}$, results in the motor velocity $\vec{V}_{MH}$. There is also a transverse force, $F_\perp$, perpendicular to the helical arc length that keeps the motor on the track. The cell membrane is assumed to stick with the cell wall. They combine into one mechanical component. The force between the motor and the membrane/wall, F_{MB}, and the one between the motor and the substrate, F_{MS}, are assumed to be purely drag forces. They act opposite to the relative velocities between the involved parts, and proportional up to a drag coefficient. The thicker arrows show the vectorial sums of the composite forces. Here we assume that the helical track is the only rotational component, whereas the cell membrane and cell wall does not rotate (constrained by much larger rotational drag coefficient). Then it holds that $\vec{V}_{HB} = r\omega_H \hat{\theta}$ and $\vec{V}_{BS} = V_C \hat{z}$, where V_C is the cell velocity and ω_H is the angular velocity of the helix rotation. $\hat{z}$ and $\hat{\theta}$ are same as in (A), $\hat{s}$ is the unit vector tangent to the direction of the helix.

A net driving force is generated when the two strands of the track bear different numbers of motors carrying the high-drag vs. low-drag cargo. This can be realized by exchanging the cargo at different rates as the motors arrive at the poles. At the leading pole the motors tend to shed the low-drag cargo and take on a high-drag one, and vice versa at the trailing pole. Then more high-drag motors will travel from the leading pole to the trailing pole than in the opposite direction. Thus the net force on the cell drives it towards the leading pole. In other words, the relative cargo exchange rates at the poles determine the direction of cell motion. When the rates switches, the cell reverses.

The simplest way to control the cell reversal is to deplete one or both types of cargo at the poles. Due to the unbalanced cargo exchange rates, the leading pole tends to accumulate low-drag motors and lose high-drag ones, and vice versa for the trailing pole. Although this mechanism makes a working model (result not shown), it has been disproven by recent experiments. A mutant motor with its proton channel deleted will lose traction on the helical rotor and cease transporting cargo pole to pole. Cells with such a mutation, nevertheless, maintain the periodic switching of the AMRP concentrations at the poles, and the alternation frequency is unaffected (Sun, Wartel et al. 2010). Therefore, the cell reversal must be controlled by biochemical oscillators at the poles that are coupled via diffusion. Indeed, the diffusion time scale fits with the recovery time scale for AMRP concentrations. The details of the oscillator will be discussed below.

The basic assumptions of the mechanical model are:

1. Motors run in a uniform direction along the track, i.e. opposite directions relative to the substrate when on opposite strand of the double helix.
2. Motors carry either high-drag or low-drag cargo. The high-drag cargo encounters very high drag at the substrate interface, and contributes to the major force generating units.
3. Motors exchange cargo at the poles, with different exchange rates so as to achieve unequal distribution of the high-drag and low-drag motors on the two strands.
4. Cells reverse when the relative cargo exchange rates switch at the poles.

Force balance

In the idealized scenario, the axial forces contribute only to the translocation of the cell, and the azimuthal forces contribute only to the rotation of the helical track. Underlying is the assumption that the helical track is rigid and undeformable, and the only significant rotation is between the helix and the cell membrane. The latter holds when in the rotational direction the drag coefficient between the helix and the cytoplasm is much smaller than those between all the other components, e.g. between cell and substrate, between cell membrane and cell wall, etc. In reality, the cell may rotate slightly relative to the substrate, but such rotation has not been well characterized in the experiments.

Figure 3-1C shows the force balance on each motor. The forces indicated in all the three panels must sum to zero. The subscript M stands for motor, B for membrane/wall, S for substrate, and H for helix. For simplicity we assume that the cell membrane and cell wall are held together with no relative motion. They are regarded as one mechanical part in the model. The motor exerts a constant force, F_M, on the track along its arc length. The track imposes an equal and opposite

force on the motor, resulting in a velocity $\vec{V}_{MH}^{i}$ to be determined by the force balances. The superscript i is the index for the motors. There is also a transverse force , $F_{\perp}$, perpendicular to the arc length that keeps the motor on the track. The force exerted by the membrane/wall on the motor is assumed to be purely a drag force, $\vec{F}_{MB}^{i} = -\zeta_{MB}^{i}\vec{V}_{MB}^{i}$, where $\vec{V}_{MB}^{i} = \vec{V}_{MH}^{i} + \vec{V}_{HB}$ is the relative velocity between the motor and the membrane/wall. Here ζ_{MB}^{i} is the drag coefficient that accounts for the drag on the motor both from the cell membrane and from the cell wall. The high-drag and low-drag cargo makes the drag coefficient different. These drag forces are internal within the cell, so they only cause relative motions between cell components, i.e. rotation of the track, but not translocation of the whole cell. Similarly, the force between the motor and the substrate is written as $\vec{F}_{MS}^{i} = -\zeta_{MS}^{i}\vec{V}_{MS}^{i}$ with $\vec{V}_{MS}^{i} = \vec{V}_{MH}^{i} + \vec{V}_{HB} + \vec{V}_{BS}$. Here we assume that the drag coefficient ζ_{MS}^{i} applies only to the high-drag motor at the substrate interface and is 0 otherwise.

Because we assume that only the track rotates, it holds that $\vec{V}_{HB} = r\omega_{H}\hat{\theta}$ and $\vec{V}_{BS} = V_{C}\hat{z}$, where r is the radius of the cross section of the cell, V_C is the cell velocity, ω_H is the angular velocity of the helix rotation. $\hat{z}$ and $\hat{\theta}$ are unit vectors in the axial and rotational direction respectively. The force balance is:

$$\vec{F}_{//}^{i} + \vec{F}_{\perp}^{i} + \vec{F}_{MB}^{i} + \vec{F}_{MS}^{i} = 0 \tag{3.1}$$

We assume that the motor-helix force parallel to the helix is constant (Eq.(3.2)). In the bacterial flagellar motor nearly constant torque is observed up to a "knee" velocity (Berg and Turner 1993; Berg 2003). Here we are essentially assuming that the motors are always functioning in the low velocity regime where the motor torque is nearly constant.

$$\sigma_{i}\vec{F}_{//}^{i} \cdot \hat{s} \equiv F_{M} \tag{3.2}$$

where $\sigma_i(t) = \pm 1$ indicates the direction of the motion relative to the substrate, i.e. which strand of the double helix the motor is currently on.

Since the motors are confined to the track, $\vec{V}_{MH}^{i}$ is proportional to ds^i/dt, where s^i is the position of the motor in arc length along the track. That is,

$$\vec{V}_{MH}^{i} = \sigma_{i}(t)\frac{ds^{i}}{dt}\left(\frac{p\hat{z}}{\sqrt{p^{2}+(2\pi r)^{2}}} + \frac{2\pi r\hat{\theta}}{\sqrt{p^{2}+(2\pi r)^{2}}}\right) \tag{3.3}$$

Finally, we must specify the force balance on the rotating track and the translocating cell. The track rotation results from the sum of rotational forces on the helix as shown in Eq.(3.4):

$$\begin{aligned}\zeta_{Hrot}\omega_{H} &= -\sum_{i}\left(\vec{F}_{//}^{i} + \vec{F}_{\perp}^{i}\right)\cdot\hat{\theta} \\ &= \sum_{i}\left(\vec{F}_{MB}^{i} + \vec{F}_{MS}^{i}\right)\cdot\hat{\theta} \\ &= -\sum_{i}\left(\zeta_{MB}^{i} + \zeta_{MS}^{i}\right)\left(\sigma_{i}\frac{ds^{i}}{dt}\frac{2\pi r}{\sqrt{p^{2}+(2\pi r)^{2}}} + r\omega_{H}\right)\end{aligned} \tag{3.4}$$

38

The cell translocation is driven by the sum of axial forces on the external medium, as shown in Eq.(3.5). Internal forces, $\vec{F}_{MB}^{\,i}$, do not count.

$$\zeta_C V_C = \sum_i \vec{F}_{MS}^{\,i} \cdot \hat{z}$$

$$= -\sum_i \zeta_{MS}^i \left(\sigma_i \frac{ds^i}{dt} \frac{p}{\sqrt{p^2 + (2\pi r)^2}} + V_C \right) \tag{3.5}$$

The parameters used in the mechanical model are listed in Table 3-1. Most of them are estimated as given in the rightmost column of Table 3-1. The rest are adjusted to reproduce the experimental data. We will demonstrate the computed results after we introduce the biochemical oscillators in the next section.

Table 3-1: Parameters used in the mechanical model.

Parameters	Meaning	Values	Source
N	number of motors	100	
F_M	motor force along the helical direction	1 pN	150 pN·nm torque of BFM stator[1] $\div$ 20 nm radius of BFM rotor[2] $\approx$ 7 pN
ζ_{MB}^L	drag coeff. between motor and membrane/wall for low-drag motor	0.1 pN·s/μm	$k_B T \div 0.04$ μm^2/s diffusion coeff. of proteins on plasma membrane[3]
ζ_{MB}^H	drag coeff. between motor and membrane/wall for high-drag motor	0.5 pN·s/μm	$> \zeta_{MB}^L$
ζ_{MS}	drag coeff. between the high-drag cargo and the substrate for high-drag motor	200 pN·s/μm	
φ	range of angle considered as substrate interface [-φ/2, φ/2]	$\pi/15$	width of AglZ clusters in the fluorescence images[4]

---

[1] See Reid, Leake et al. 2006; Sowa and Berry 2008.
[2] See Sowa and Berry 2008.
[3] See Adams, Chen et al. 1998; Lippincott-Schwartz, Snapp et al. 2001.
[4] See Mignot, Shaevitz et al. 2007.

ζ_C	translocation drag coeff. of the cell	2000 pN·s/µm	100 pN pilus force[5] ÷ 3 µm/min cell velocity
ζ_{Hrot}	rotational drag coeff. of the track	50 pN·s	
p	pitch of helix	1 µm	MreB pitch[6]
r	radius of helix	0.2 µm	AglZ 3D localization[7]

Biochemical oscillators at the cell poles govern the periodic reversal

In this section we describe a biochemical scheme in which the master oscillators at the poles cause periodic changes in the cargo concentrations. The two cargo types tend to concentrate at opposite poles. Motors arriving at the pole take up a high-drag or low-drag cargo with probabilities depending on their relative concentrations at the pole. While the leading pole tends to supply high-drag cargo, the trailing pole tends to supply low-drag cargo.

Because there is not enough information about the biochemical pathway at the cell poles, we borrowed the master oscillator from existing models. The Min oscillator is one of the best studied biochemical oscillators emerging from diffusion-reaction mechanisms (Howard, Rutenberg et al. 2001; Howard and Kruse 2005; Fischer-Friedrich, Meacci et al. 2010). Since the details of the oscillator are not important, we chose the simplest form of the existing Min models (Howard, Rutenberg et al. 2001), and rescaled the parameters to achieve an oscillation period around 7 min ×2 (7 min is time between reversals, i.e. the half period) in a 5 µm long cell. We emphasize that any pair of limit cycle oscillators coupled by diffusion will work (e.g. the Fitzhugh-Nagumo system). The Min oscillator gives a more realistic biochemical flavor as the cell reversal is apparently controlled by diffusion coupled oscillations.

The original equations for the Min model (Eq.(1-4) in (Howard, Rutenberg et al. 2001)) are:

$$\frac{\partial \rho_D}{\partial t} = D_D \frac{\partial^2 \rho_D}{\partial x^2} - \frac{k_1 \rho_D}{1 + K_{m1}\rho_e} + k_2 \rho_e \rho_d \tag{3.6}$$

$$\frac{\partial \rho_d}{\partial t} = \frac{k_1 \rho_D}{1 + K_{m1}\rho_e} - k_2 \rho_e \rho_d \tag{3.7}$$

$$\frac{\partial \rho_E}{\partial t} = D_E \frac{\partial^2 \rho_E}{\partial x^2} - k_3 \rho_D \rho_E + \frac{k_4 \rho_e}{1 + K_{m4}\rho_D} \tag{3.8}$$

---

[5] See Maier, Potter et al. 2002.

[6] See Mauriello, Mouhamar et al. 2010. In the paper the pitch was stated as 0.5 µm. But it actually refers to the spacing between the two strands of helices. Thus the pitch of a single helix is 1 µm.

[7] Sun and Shaevitz, unpublished data.

$$\frac{\partial \rho_e}{\partial t} = k_3 \rho_D \rho_E - \frac{k_4 \rho_e}{1 + K_{m4} \rho_D} \tag{3.9}$$

Eqs. (3.6)-(3.9) can be non-dimensionalized by the cell length L, and the diffusion coefficients D_D and D_E (Table 3-2). The Min model in (Howard, Rutenberg et al. 2001) gives an oscillation period around 110s. A new oscillation period ~880s is obtained by scaling all the parameters with $L = 5$ μm and the diffusion coefficients reduced by 20%. The characteristic particle densities, n_D and n_E, do not affect the oscillation period. They are normalized to 1 for convenient comparison of the rate constants. The scaling and values of the parameters are given in Table 3-2. The result is shown in Figure 3-2A.

The MinE concentrations are abstracted from the rescaled Min model at the boundaries, $x = 0$ and $x = L$, and used as the master oscillators (Figure 3-2B). The master oscillators are anti-phased at opposite poles, and the alternating pattern controls the periodic reversal of the cell.

Table 3-2: Rescaled parameters of the Min model.

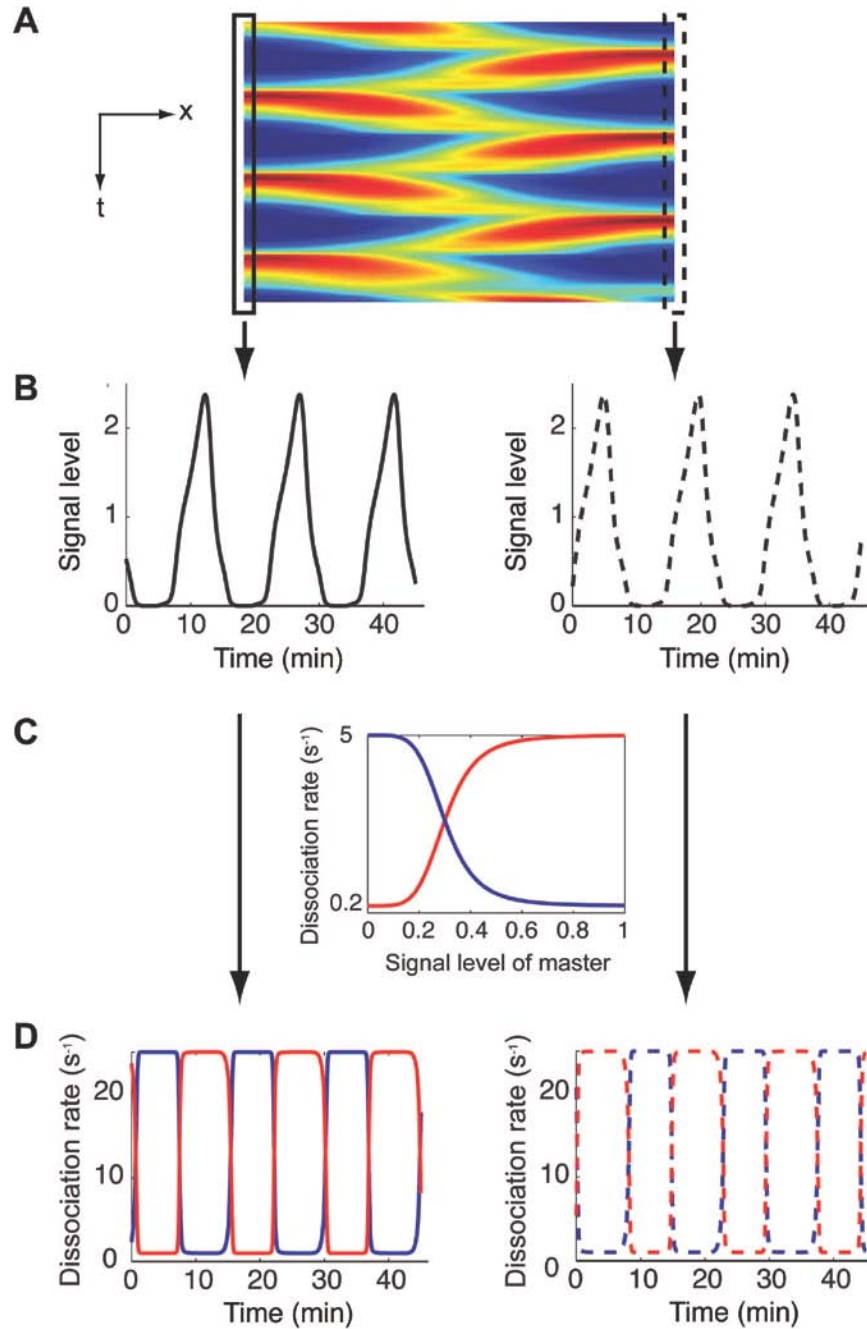| Parameters	Scaling	Values
L	$\times 2.5$	5 μm
D_D	$\times 0.8$	0.224 μm^2/s
D_E	$\times 0.8$	0.48 μm^2/s
n_D	$\div 1500$ μm^{-1}	1
n_E	$\div 85$ μm^{-1}	1
k_1	D_D / L^2	2.56 s^{-1}
k_2	$D_D / n_E L^2$	0.0685 s^{-1}
k_3	$D_E / n_D L^2$	7.68 s^{-1}
k_4	D_E / L^2	0.1024 s^{-1}
K_{m1}	$1 / n_E$	2.38
K_{m2}	$1 / n_D$	40.5

Figure 3-2: Biochemical signals at the cell poles. (**A**) Kymograph (i.e. space-time plot) showing the bound MinE concentration computed from the rescaled Min model. See Table 3-2 for the rescaled parameters. (**B**) The time series of boundary concentrations are extracted from the Min model to be used as the master biochemical oscillators at the poles. The oscillations at the two poles are anti-phased. The master oscillators set the periodicity of the cell reversal. (**C**) The sigmoidal filter that translates the signal of the master oscillators into the dissociation rates of the cargo at the poles. The high-drag and low-drag cargo have opposite trends in their responses to the master oscillators. (**D**) The

42

dissociation rates of the cargo at the poles vs. time. After the sigmoidal filter in (C), the sharp signal of the master oscillator turns into nearly square waves. The high-drag and low-drag cargo alternate their binding affinity at each pole with the periodicity set by the master oscillators. This will result in the periodic switch of their relative concentrations at the poles, and eventually the cell reversal. In (B), (C) and (D), red: high-drag cargo, blue: low-drag cargo. In (B) and (D), solid line: left pole, dashed line: right pole.

The master oscillators peak sharply, whereas the AMRPs concentrations are nearly constant between reversals. Therefore, we used sigmoidal signal filters (Eqs.(3.10) and (3.11), Figure 3-2C) that convert the master signal into nearly square waves (Figure 3-2D). Sigmoidal signal-response curves are common in cooperative biochemical reactions. The signal filters for the high-drag and low-drag cargo assume opposite trends, so that they tend to accumulate at opposite poles. The filtered waves are applied as the dissociation rates of the high-drag and low-drag cargo at the poles. Figure 3-2D shows that the dissociation rates of the cargo oscillate in anti-phase at the two poles; and the rates for high-drag and low-drag cargo dominate at opposite poles.

$$r_H = r_{\min} + (r_{\max} - r_{\min}) \frac{S^n}{S^n + Q_H^n} \tag{3.10}$$

$$r_L = r_{\min} + (r_{\max} - r_{\min}) \frac{Q_L^n}{S^n + Q_L^n} \tag{3.11}$$

In Eqs.(3.10) and (3.11), r_H and r_L are the dissociation rates of the high-drag and low-drag cargo respectively. $r_{\min} = 0.2$ s^{-1} and $r_{\max} = 5$ s^{-1} sets the lower and upper bound of the dissociation rates. S is the signal of the master oscillator. The Hill coefficient $n = 5$ and the half-rate signal level $Q_H = Q_L = 0.3$.

Subsequently, the cargo concentrations at the poles are determined by the periodically changing dissociation rates, together with a constant binding rate and diffusion through the cytoplasm (Figure 3-3B). The ratio between the concentrations of the two cargo types determines the probability that an incoming motor takes up a high-drag or low-drag cargo. Here we postulate one possible mechanism for the above process. Some cargo exchange enzymes docked at the poles sequester the free cargo for exchange with the incoming motors. Their binding affinity for high-drag or low-drag cargo is controlled by the master oscillator in the sigmoidal fashion described above.

Eqs.(3.12) below capture the diffusion coupled dynamics of the high-drag cargo at the poles: (a) the diffusion of the cargo in the cytoplasm; (b) and (c) the balance of diffusive fluxes with reaction fluxes at the poles; (d) and (e) the dynamics of the bound cargo at the poles. The equations for low-drag cargo read similarly. In Eqs.(3.12), $H_c(t, x)$ is the cargo density in the cytoplasm, $H_p^0(t)$ is the cargo concentration at the left pole $x = 0$, $H_p^L(t)$ is the cargo concentration at the right pole $x = L$. $D = 2$ μm^2/s is the diffusion coefficient of cargo. $r_b = 5$ μm/s is the binding rate of cargo, $r_H^0(t)$ and $r_H^L(t)$ are the dissociation rates computed above. $M_H^0(t)$ and $M_H^L(t)$ are the fluxes of cargo from the cargo exchange with the motors.

$$
\begin{cases}
\dfrac{\partial H_c}{\partial t} = D\dfrac{\partial^2 H_c}{\partial x^2}, & 0 < x < L & \text{(a)} \\[2ex]
D\dfrac{\partial H_c}{\partial x} = -r_H^0(t)H_p^0 + r_b H_c, & \text{at } x = 0 & \text{(b)} \\[2ex]
D\dfrac{\partial H_c}{\partial x} = r_H^L(t)H_p^L - r_b H_c, & \text{at } x = L & \text{(c)} \\[2ex]
\dfrac{dH_p^0}{dt} = -r_H^0(t)H_p^0 + r_b H_c(t,0) + M_H^0(t) & & \text{(d)} \\[2ex]
\dfrac{dH_p^L}{dt} = -r_H^L(t)H_p^L + r_b H_c(t,L) + M_H^L(t) & & \text{(e)}
\end{cases} \tag{3.12}
$$

Results of the model explain most experimental observations

The model explains most existing experimental data. The most important results of the model are summarized in Figure 3-3. Figure 3-4 shows the time lapse snapshots of the motor and cargo distributions during cell translocation, viewed from the top. Supplemental Video I give side-view movies of the reversal cycle, and Supplemental Video II gives a slowed-down zoomed-in movie for a short time period about the cell reversal.

The computed cell velocity is ~3.4 µm/min (blue solid line in Figure 3-3A), falling in the range of 2−4 µm/min from experiments. The cell rotates at a speed ~3.7 rpm (green dashed line in Figure 3-3A). For cells suspended in soft medium, the computed rotational speed of the track is ~7.2 rpm (see Appendix A), compatible with the measured 7−8 rpm in cells immersed in methylcellulose. Controlled by the master oscillators, the cell translocation and the track rotation reverses periodically for every 7 min.

Upon reversal the cell slows down to near stall (inset of Figure 3-3A), corresponding to the 10-sec pause observed in the experiments. This occurs because the motors have to redistribute along the helix. Before the reversal, the major force-generating units, i.e. motors carrying high-drag cargo, dominate in the direction bound for the trailing pole (Figure 3-3C). Upon reversal, the poles switch and high-drag motors start to dominate in the direction towards the new trailing pole. This causes a transition period during which the numbers of high-drag motors become more balanced in the two directions (Figure 3-4), and the driving forces largely cancel out. If we take into account the viscoelastic property of the slime surrounding the cell, the cell should virtually stop when the driving force per unit area drops below the yield stress of the slime, as in the short pauses shown in the experiments (Mignot, Shaevitz et al. 2007).

The dynamics of the AMRP clusters along the cell-substrate interface are well explained by the model. The motors carrying high-drag cargo cluster at the substrate interface (Figure 3-3C and Figure 3-4) because they are slowed down there (Figure 3-3D). The clusters are localized along the helical strand that currently supports the leading-to-trailing motion; they are equally spaced by the pitch of the helical track. Occasionally a motor picks up a high-drag cargo from the trailing pole, and is slowed down at the substrate interface as it runs towards the leading pole. Nevertheless, with the probability being small, such a motor can hardly find companions to form cluster before it reaches the other pole. The high-drag clusters drift towards the trailing pole with

a much smaller velocity than the cell velocity, ~0.3 µm/min. Such a small drift is hardly distinguishable in experiments because of the fluctuations in fluorescence. The drift velocity is affected by many parameters, but mainly by ζ_{MS}, the drag coefficient between the high-drag motor and the substrate (see Appendix B). Increasing this drag coefficient reduces the drift velocity. An extremely large drag coefficient would correspond to the case when the high-drag cargo binds to the substrate.
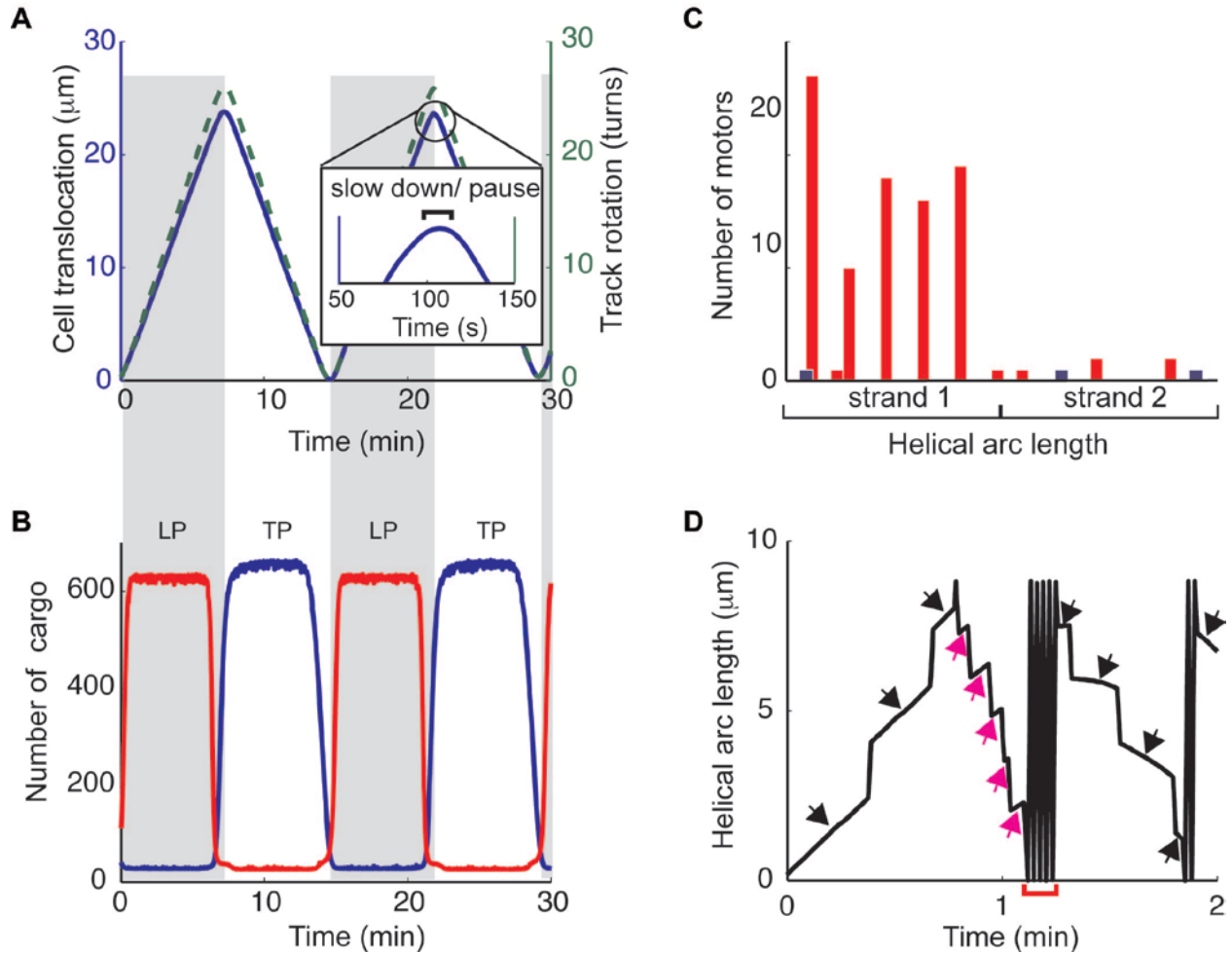

Figure 3-3: The results of the calculations. Parameters used in the calculation are listed in Table 3-1. (**A**) The time trajectories of the cell translocation (*blue solid line, left axis*) and the track rotation (*green dashed line, right axis*). The translocation and rotation show periodic reversal with synchronized phases. The cell moves at ~3.4 µm/min and the track rotates at ~3.7 rpm. The inset with zoomed-in view around the reversal shows a short interval of nearly zero velocity. (**B**) The dynamics of the cargo concentrations at the right pole. The left pole behaves exactly the opposite. Red: high-drag cargo; blue: low-drag cargo. The grey blocks highlight the time intervals in which the right pole is the leading pole (positive cell velocity). The high-drag cargo concentrates at the leading pole (LP) and the low-drag cargo concentrates at the trailing pole (TP). The cargo concentrations

result from the oscillating cargo binding affinity, which is controlled by the master oscillators. For most time between cell reversals, the cargo concentrations stay around the equilibrium level. Small noise around the equilibrium densities are caused by the cargo exchange for motors arriving at the pole. (**C**) The distribution of motors along the track at a sample moment. Red columns: number of high-drag motors; blue columns: number of low-drag motors. The high-drag motors form equidistant clusters (*tall red columns*). Most high-drag motors run from the leading pole to the trailing pole, because the leading pole tends to equip the motors with high-drag cargo. So the clusters only appear on the helical strand that supports the leading-to-trailing motion at the moment. Due to the significantly reduced velocity in the clustered regions, most motors are trapped there, with only a small number of motors distributed elsewhere. (**D**) A sample time trajectory of a single motor along the track. The motor travels many times pole to pole before the cell reverses. The slowed-down parts (*black arrows*) are caused by high-drag cargo through the substrate interface. This tends to happen in the leading-to-trailing direction. Before the cell reversal (*red bracket*), the slowing-down mostly happens on the upward slope towards the old trailing pole; and after the cell reversal, the slowing-down shifts to the downward slope towards the new trailing pole. In the rare event that the motor carries the high-drag cargo towards the leading pole, it lags slightly on the track (*magenta arrows*) because the helix rotation takes over the motor while it is held behind by the substrate interface. Around the cell reversal, motor trajectories become more erratic because the switch in cargo exchange rates is underway.

The polar concentrations of the cargo reproduce the oscillatory pattern of AMRP polar clusters. The high-drag cargo always concentrates at the leading pole and the low-drag cargo always concentrates at the trailing pole (Figure 3-3B). For most of the time between reversals, the polar concentrations of the cargo maintain nearly an equilibrium level determined by the binding and dissociation rates. The cargo exchange kinetics is an additional source of fluctuations about the equilibrium level. At each reversal, it takes ~1 minute for the cargo concentrations to reset, which spans before and after the mechanical reversal. This duration depends on the kinetics of the chemical process, e.g. the binding and dissociation rates, the diffusion coefficient of the cargo, the sharpness of the sigmoidal filter. During the delay, most cargo particles disperse in the cytoplasm (data not shown), and the concentrations sequestered at both poles are low. But the mechanical reversal does not have to wait until the polar concentrations of cargo fully reset. It happens soon after the ratio between the two cargo types reaches 1, up to the pause time needed for motor redistribution. Thereby the polar clustering seems to form about 20 seconds after the cell has reversed, which was observed in experiments (Mignot, Shaevitz et al. 2007). It is tempting to associate the temporal order with causality. But this case is exactly opposite: the mechanics is controlled by the cargo concentrations.

The various AMRPs observed in the experiments are probably constituents of the high-drag or low-drag cargo. For example, AglZ, which accumulates at the leading pole and forms equidistant clusters along the body, should be part of the high-drag cargo. RomR, which accumulates at the trailing pole, is part of the low-drag cargo (Leonardy, Freymark et al. 2007). FrzCD, which seems to interdigitate with AglZ along the cell body, is also likely to be part of the low-drag cargo.
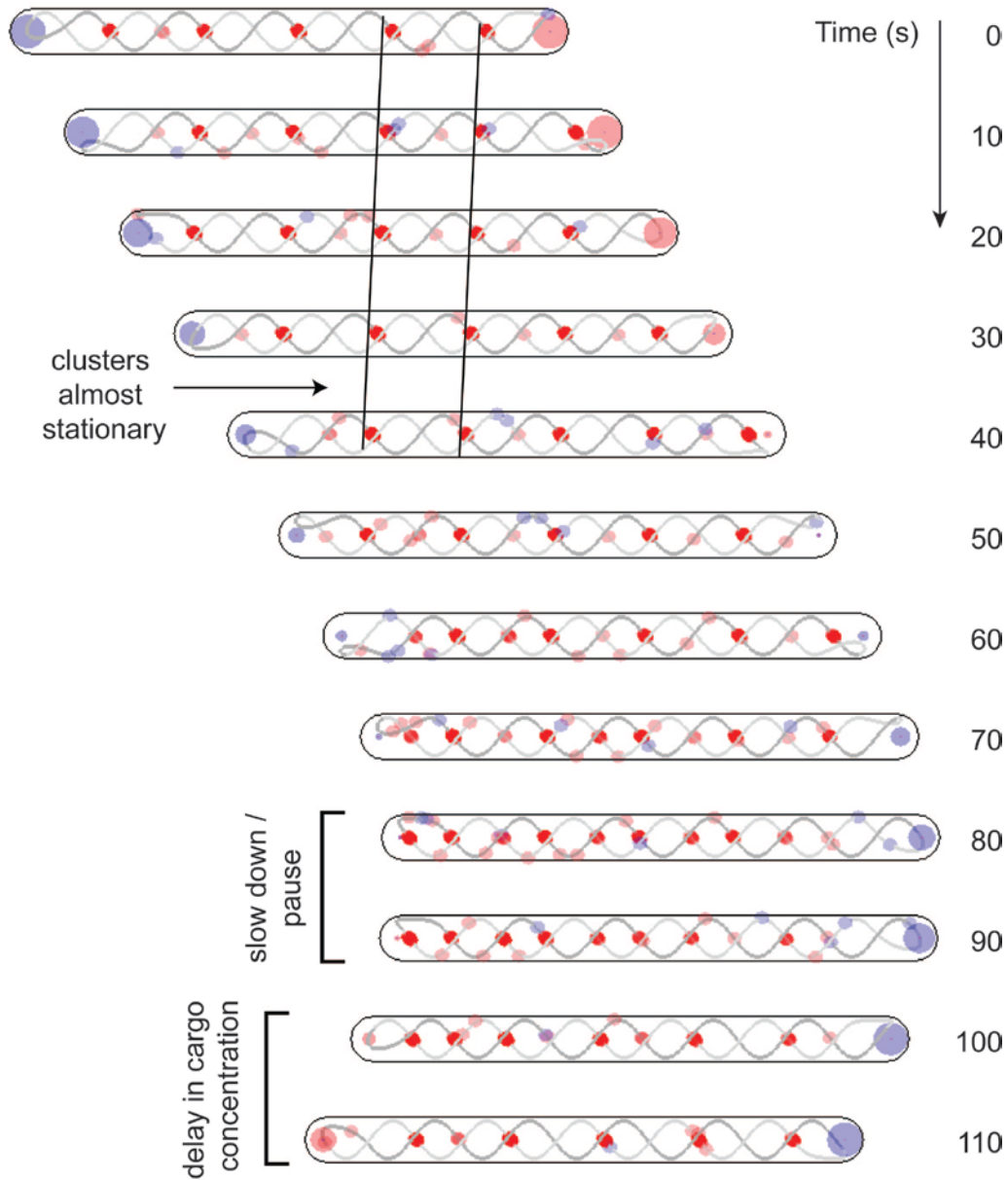
Figure 3-4: Time lapse snapshots of a computed cell viewed from the top. See Supplemental Video I and II for movies with side view. Black oblongs: cell envelope; grey lines: helical track; blue balls along the track: motors carrying low-drag cargo; red balls along the track: motors carrying high-drag cargo; blue ball at the pole: polar low-drag cargo, radius proportional to concentration; red ball at the pole: polar high-drag cargo, radius proportional to concentration. The balls indicating the motors are semi-transparent. When clustered, they appear like one ball with brighter color. The motors carrying high-drag cargo slow down and form clusters at the substrate interface. The clusters are equally spaced by the pitch of the helical track. They move relatively to the substrate much slower than the cell does — in this computation, at ~0.3 μm/min. Before cell reversal the density of high-drag cargo disperses at the old leading pole and after cell

47

reversal re-accumulates at the new leading pole with a ~20 s delay. The changes in low-drag cargo are similar, but not exactly symmetric to the dynamics of the high-drag cargo because the master oscillator from the Min model does not behave symmetrically in the high and low regime (Figure 3-2B). During the reversal, the motors carrying different cargo redistribute along the track. The cartoon compares well with the AglZ-GFP imaging experiments reported in (Mignot, Shaevitz et al. 2007).

3.3 Discussions

We have constructed a model that explains the mechanics of A-motility in myxobacteria. The basic elements consist of proton driven motors running along a double helical track. The forces in the axial direction drive the translocation of the cell; and the forces in the rotational direction drive the rotation of the track. The motors are loaded with high-drag or low-drag cargo. The motors carrying high-drag cargo encounter large drag forces at the substrate interface. They are significantly slowed down there and form clusters. These high-drag motor-cargo complexes constitute the major force generating units in the system. Most of them run from the leading pole towards the trailing pole. They exert a net forward thrust on the cell. The motor exchanges its cargo when it reaches the cell pole. The type of cargo it picks up depends on the concentrations of the two types at the pole, so that the motors sent out from the leading pole tend to carry the high-drag cargo and vice versa. The cargo concentrations are controlled by the master oscillators at the pole. The master oscillators set the periodicity for reversal of the cargo concentrations and consequently the cell motion. The model reproduces the translocation velocity of the cell and the rotational velocity of the track observed in the experiments. It explains the equidistant, nearly stationary clustering of cargo AMRPs along the cell-substrate interface and the AMRP concentration at the poles as well. It also explains why the cell pauses shortly before the reversal and why the AMRP concentrations rebuild at the poles after the reversal even though they control the mechanics. The model mainly deals with the mechanical aspects of A-motility. The biochemistry is a simple diffusion coupled binding-unbinding process grafted onto the Min oscillator model. Before more details are known about the signaling pathways, the current model is the best one can do to mimic the observed AMRP dynamics.

The model predicts a linear load-velocity curve. Figure 3-5 shows the cell velocities resulting from a range of external load forces against the cell motion. The cell stalls when the load reaches ~150 pN. The zero-load velocity and the stall force vary with the model parameters. There are many ways to measure load-velocity curves experimentally. The external load force can be applied on the cell directly or indirectly through covalently attached micro-beads, using atomic force microscopy (AFM), optical tweezer, flow chamber, etc.

In this model it is necessary to assume two types of cargo. In the model setup, we mentioned that symmetry breaking in the mechanical system can come from unequal number of motors in the two directions and/or unequal forces. The cargo assumption in this model corresponds to unequal forces. Suppose otherwise, i.e. there is only one type of motor-cargo and more motors run leading-to-trailing than the opposite direction. Then one should observe strong and weak AMRP clusters interdigitating along the cell body, formed by the motors in the two directions respectively — unless there are no motors running from the trailing to the leading pole. But if there are no trailing-to-leading motors, the FrzCD bands that interdigitate with the AglZ band

would be difficult to explain. In contrast, assuming two cargo types easily reconciles this contradiction. In the current model the numbers of motors in the two directions are not balanced either, because the high-drag motors are slowed down at the substrate interface, creating a much longer average travel time in the leading-to-trailing direction (Figure 3-3D).

It is likely that the AMRPs behave in a more complicated way than simply as two cargo types. For example, RomR and FrzCD both seem to be low-drag cargo, yet differ in their polar affinity: RomR concentrates at the trailing pole, but FrzCD does not concentrate at either pole. This suggests further differentiation in the interactions between the motor and the AMRPs. High-drag and low-drag cargo is the simplest working scheme that explains the major dynamical pattern observed in experiments.
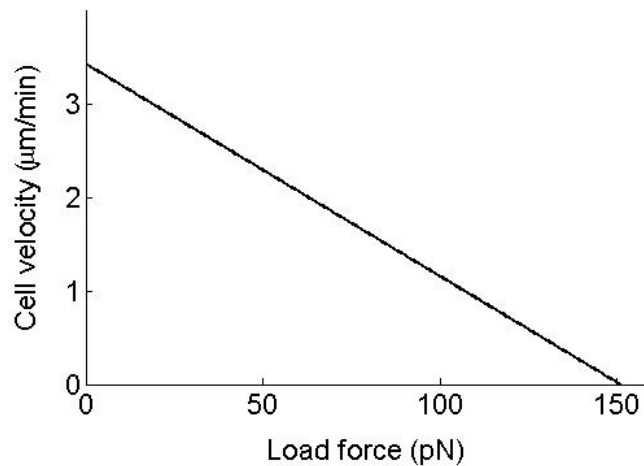

Figure 3-5: Load-velocity curve predicted by the model. The cell velocity decreases linearly with increasing external load force. The stall force is ~150 pN. The curve can be approximated by $V = 3.4 - 0.23 \times F_L$.

Recent experiments suggest that the motor-substrate interaction is more complicated than high resistance to cargo-induced surface bumps. In our model the substrate-induced clustering emerges solely from the slowing-down of the motors carrying high-drag cargo. This is a convection dependent mechanism. If the motors cease their directional motion, pure diffusion along the track cannot lead to cluster formation even though their diffusion coefficients are reduced at the substrate interface (see Appendix C). However, recent experiments show that the AMRP clusters remain in mutant cells with the proton channel deleted from the motors (Sun, Wartel et al. 2010). One possible remedy to the model is to introduce kinetic binding between the cargo and the substrate. In this case clusters of motor-cargo form in regions of reduced diffusive mobility (see Appendix C). The binding mechanism is not exactly the same as the usual focal adhesion mechanism, and so it may not require the enzymatic degradation of the cell wall. The cluster formation only depends on the equilibrium ratio between the cargo bound and unbound to the substrate. If the binding and unbinding happens fast enough, each time the bonds can reform across the porous peptidoglycan without cutting through it. Nevertheless, the additional

mechanism does not affect the essential result of the current model. In the presence of directional motor motility, the cell velocity is mainly determined by the force generated by clustered high-drag motors and their residence time through the clusters. The binding mechanism effectively contributes to a longer residence time. Its impact on the cell velocity can be modeled by adjusting the drag coefficient between the high-drag cargo and the substrate.

In the current model, the mechanics only affects the biochemistry by introducing small concentration fluctuations. But more substantial mechanochemical coupling probably exists. In the "ripple phase", the cells reverse with higher frequency when they interdigitate with other cells moving in the opposite direction. The neighboring cells essentially form a new "moving substrate" for each other. Thus the motors may take a longer or shorter time to travel pole-to-pole, and so does the cargo. If some components of the cargo participate in the biochemical oscillators, the impact on their transportation may affect the oscillation period. Even in the Min model, there is recent evidence for mechanical feedback on the biochemistry (Ivanov and Mizuuchi 2010). Again, all these speculations await further experiments for more details of the biochemical pathway.

Finally, similar motility mechanism may be widespread in bacteria since MreB homologs and MotA-MotB homologs are common across a variety of bacterial species. For example, the swimming cyanobacterium *Synechococcus* rotates about its long axis after it hits a wall, establishing a rotational component in the motility. This could be realized by motors running along helical track, as in myxobacteria A-motility. If the cell surface assumes a helical pattern, the resultant cell rotation will provide axial thrust. Alternatively, the rotation of the internal helix could generate helical waves on the bacterial surface. This would provide the mechanism for wave-driven motility postulated by Stone and Samuel (Stone and Samuel 1996) and Ehers, *et al.* (Ehlers, Samuel et al. 1996).

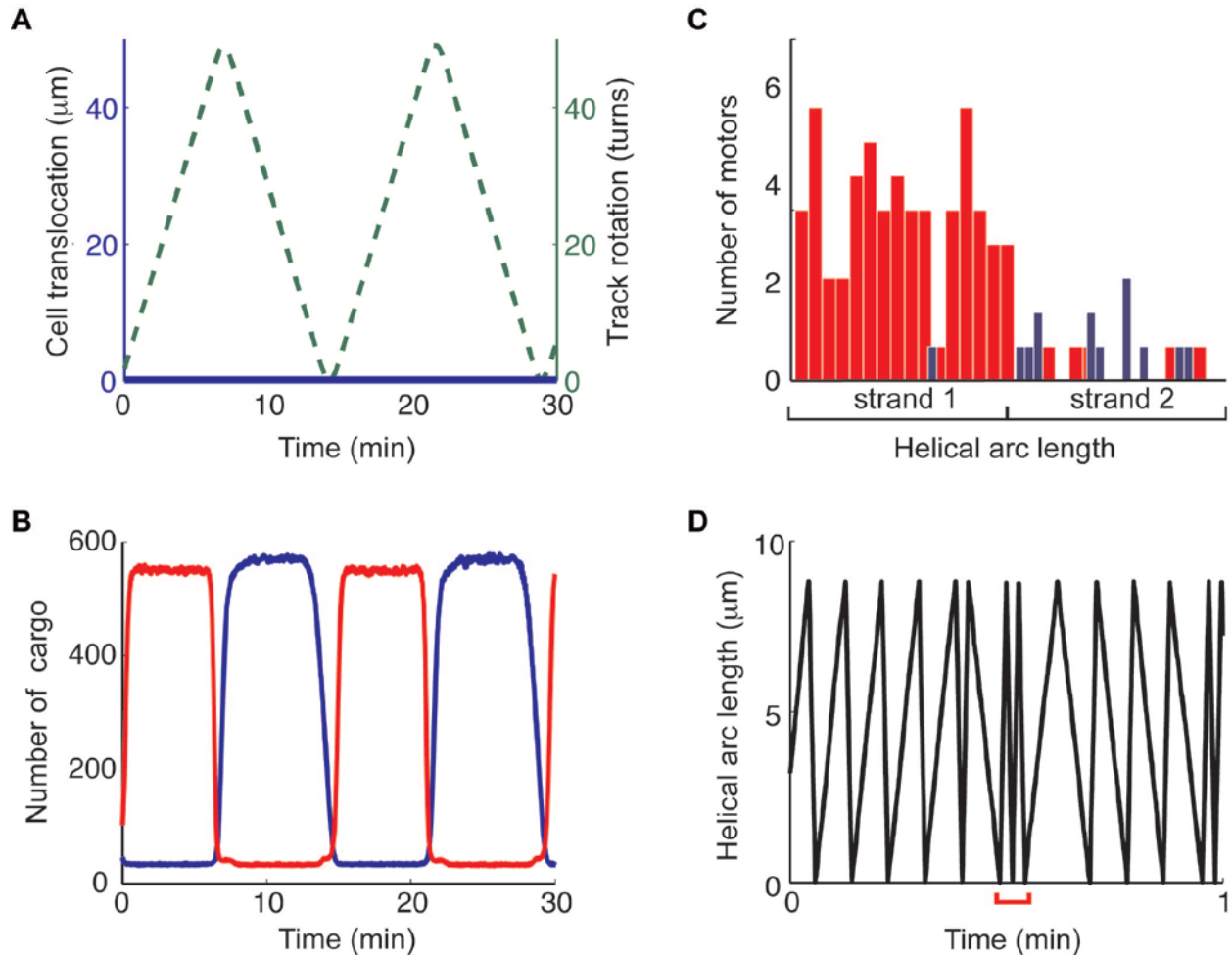# Appendix A: Results for cells suspended in methylcellulose

Figure 3-6: Results for cells suspended in methylcellulose. Parameters used in the calculation are listed in Table 3-1, except for $\varphi = 2\pi$, and $\zeta_{MS} = 0$. All the legends follow those in Figure 3-3. (**A**) The translocation of the cell (*blue solid line, left axis*) and the rotation of the helical track (*green dashed line, right axis*). The track rotates at ~7.2 rpm. The rotation maintains the periodic reversal for every 7 min or so. The cell does not translocate because there is no external forces against the methylcellulose gel with $\zeta_{MS} = 0$. (**B**) The cargo concentrations at the right-end pole. The result is similar to Figure 3-3B. (**C**) The distribution of motors along the track at a sample moment. The high-drag (*red*) motors are mostly located on one strand and the low-drag (*blue*) motors mostly located on the other, running in the opposite direction. The high-drag motors do not form clusters along the cell body. There are more high-drag motors because they move slower along the track. (**D**) A sample time trajectory of a single motor. Red bracket: cell reversal. The motors travel faster when carrying a high-drag cargo. So the trajectory is slightly asymmetric on the upward and downward slopes.
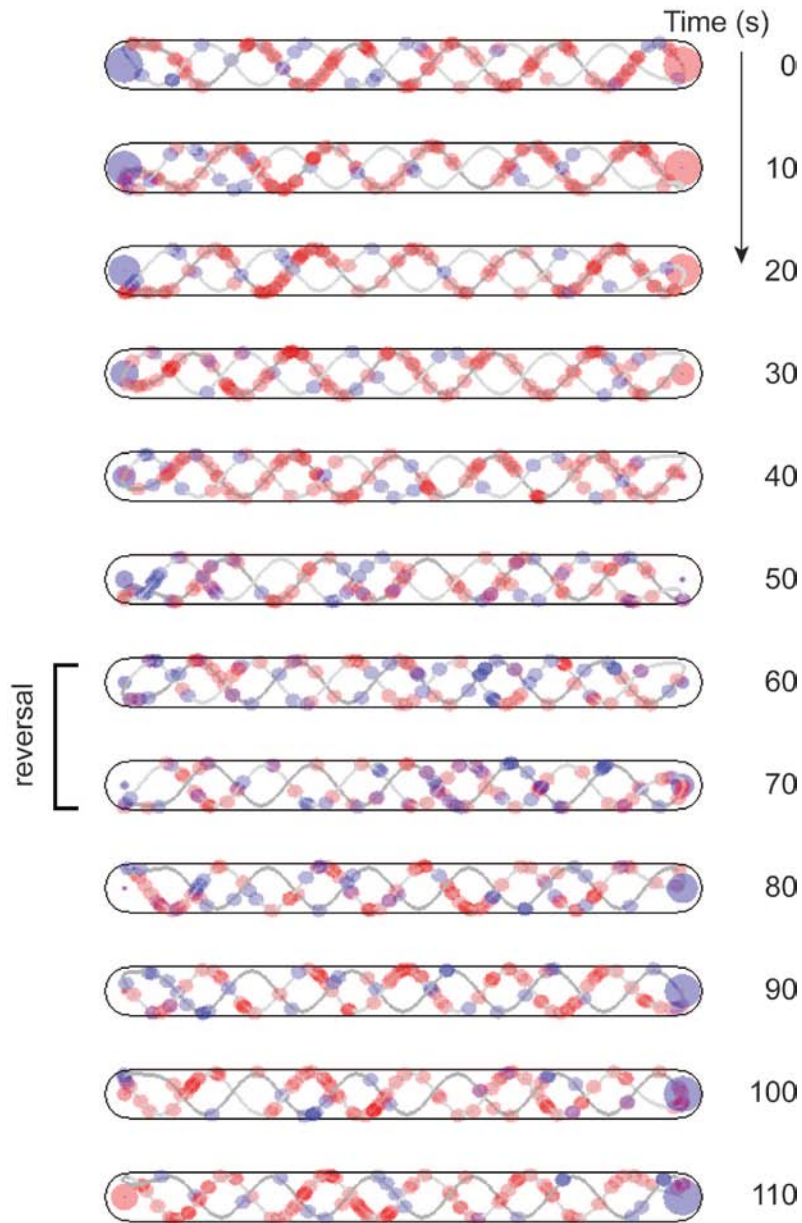
Figure 3-7: Time lapse snapshots for cells suspended in methylcellulose viewed from the top. See Supplemental Video III for movie with side view. Black oblongs: cell envelope; grey lines: helical track; blue balls along the track: motors carrying low-drag cargo; red balls along the track: motors carrying high-drag cargo; blue ball at the pole: polar low-drag cargo, radius proportional to concentration; red ball at the pole: polar high-drag cargo, radius proportional to concentration. The cargo concentration switches periodically as in the cell on substrate surface. The two helical strands are colored with different shades of grey. The high-drag and low drag motors are distributed along opposite strands. Before pole switching (around time 60 and 70 s) the high-drag motors are mainly located along the darker strand and afterwards mainly along the lighter strand; vice versa for the low-drag motors. Upon pole switching, the cargo type carried by the

52

motors redistribute on the two strands), causing the reversal of track rotation. The motors do not form clusters as those shown in Figure 3-4.

Suspension in methylcellulose inhibits the cell translocation in the axial direction, but the double helical track rotates at 7−8 rpm. Also, the AMRPs do not form clusters anywhere along the cell body. Only the poles maintain their periodic fluctuation in AMRP concentrations.

These observations are well reproduced by the model (Figure 3-6, Figure 3-7 and Supplemental Video III). The methylcellulose is a viscoelastic medium that essentially forms "super-soft" substrate all around the cell. Accordingly, in the model we change ζ_{MS} to 0. The computed rotational speed, ~7.2 rpm, is compatible with the measured 7−8 rpm. The track also reverses its direction of rotation every 7 min. The rotation occurs because the high-drag motor has a larger drag coefficient against the membrane/wall than the low-drag motor does. The difference in these internal drag forces drives the rotation of the track, but do not contribute to cell translocation. In reality there may be a small drag between the high-drag cargo and the methylcellulose, causing a small driving force for cell translocation. But the cell may remain immobile if the driving force is smaller than the yield stress of the methylcellulose.

Because the external drag coefficient is radially symmetric, in particular, zero everywhere, the high-drag motors do not form clusters (Figure 3-6C and Figure 3-7). The high-drag motors and low-drag motors mainly distribute on opposite strands. Such a distribution is caused by the unequal cargo exchange rate at the poles, as in the substrate-supported case discussed in the main text. The pole with higher concentrations of high-drag cargo tends to send out high-drag motors, and the other pole tends to send out low-drag motors. Between the reversals, there are usually more high-drag motors than low-drag ones. This is because the high-drag motors travel slower, thus by flux balance of motors they achieve higher density.

Appendix B: Model is robust against parameter change

The model behaves robustly across a wide range of parameters (Figure 3-8). The computed velocities increase linearly with motor force, F_M,. The drag coefficients between the motor and the membrane/wall, ζ_{MB}^H and ζ_{MB}^L, affect the results very little. They mainly determine the motor velocities outside the substrate interface, the region with only a small number of motors for most time between reversals (Figure 3-3C). The cell velocity and the track rotation speed vary similarly, except for varying ζ_{MS}, the drag coefficient between the high-drag cargo and the substrate. The drift velocity of the clusters equals $V_C - p\omega_H$; with the pitch $p = 1$ μm in the model, the vertical distance between the green and the blue lines in Figure 3-8 represents the drift velocity. It is strongly affected by ζ_{MS}, because ζ_{MS} characterizes the slipping between the cluster and the substrate. The limit of infinite ζ_{MS}, corresponding to fixed adhesion complexes, gives zero drift velocity.
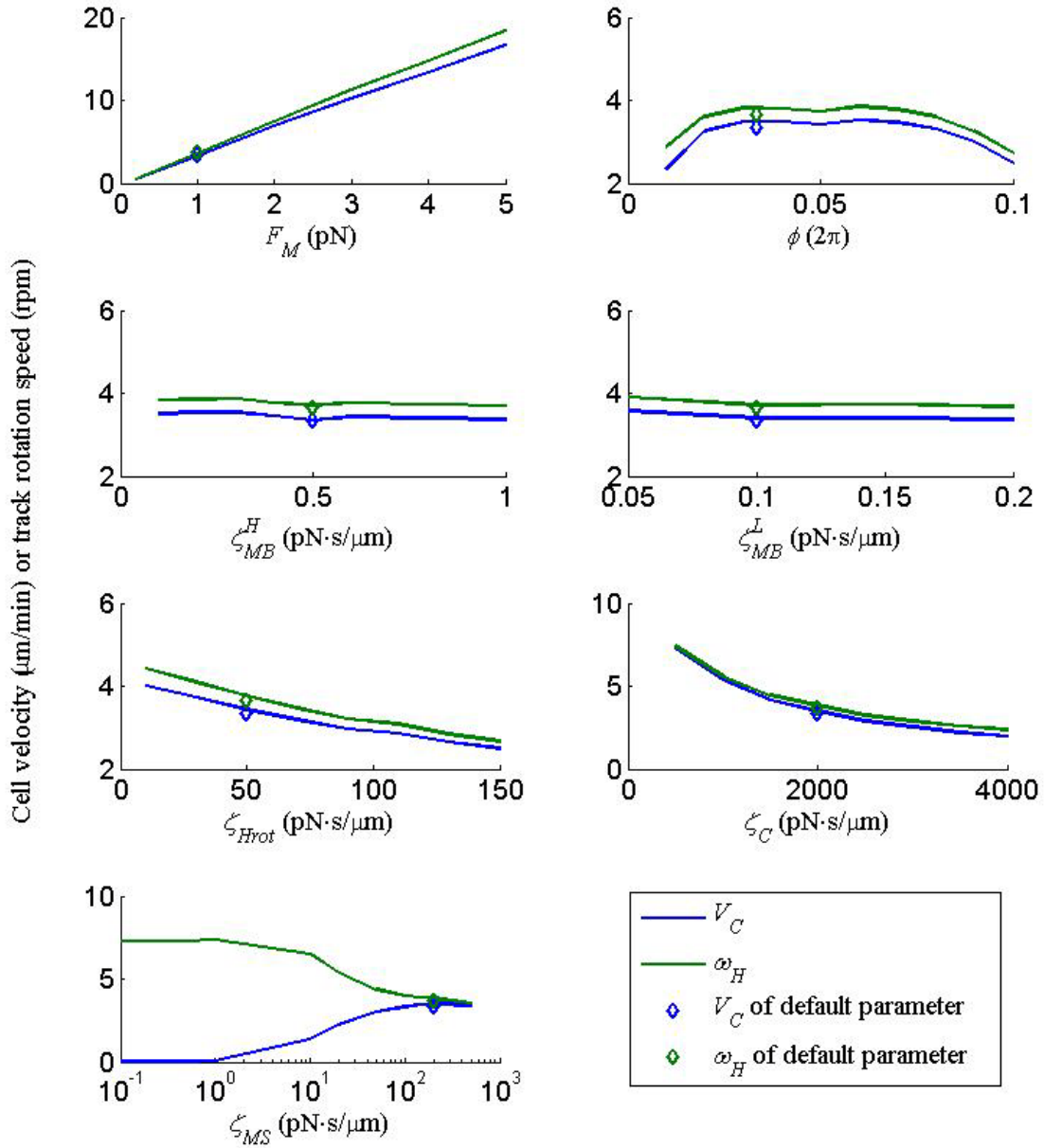
Figure 3-8: Parameter sensitivity of the cell velocity and track rotation speed.
Vertical axes in all panels: cell velocity and track rotation speed. Horizontal axes, from left to right and then up to down: motor force F_M, range of angle for substrate interface ϕ, drag coefficient between the high-drag motor and the membrane/wall ζ_{MB}^H, drag coefficient between the low-drag motor and the membrane/wall ζ_{MB}^L, rotational drag coefficient of the track ζ_{Hrot}, drag coefficient of the cell ζ_C, drag coefficient between the high-drag cargo and the substrate ζ_{MS}. The result of the model behaves robustly over the range of parameters.

54

Appendix C: Motor-substrate binding causes motor clustering under pure diffusion

In cells with mutant motors with knock-outs of its proton channel, the AMRPs remain clustered at the substrate interface. In this case the motors can only diffuse along the track. The diffusion coefficient is significantly reduced at the substrate interface for motors carrying high-drag cargo. However, clustering cannot be explained by the spatial variation in diffusion coefficient. The governing Fokker-Planck equation for the 1D diffusion process is

$$\frac{\partial \rho}{\partial t} = \frac{\partial}{\partial x}\left(D(x)\frac{\partial \rho}{\partial x}\right) \tag{3.13}$$

where x is the arc length along the track, $\rho(t, x)$ the density of motors along the track and $D(x)$ the diffusion coefficient, which is reduced at the substrate interface.

Without an energy supply, the steady state is just the equilibrium solution, i.e. zero flux everywhere. Therefore, $\partial \rho / \partial x = 0$, the motor density is constant, without any clustering.

A kinetic binding process between the substrate and the motor/cargo complex is one possible way to create the spatial variation in density. Let $k_b(x)$ and $k_u(x)$ be the binding and unbinding rates between the motor-cargo complex and the substrate. The modified diffusion PDE reads

$$\frac{\partial \rho_u}{\partial t} = \frac{\partial}{\partial x}\left(D(x)\frac{\partial \rho_u}{\partial x}\right) - k_b(x)\rho_u + k_u(x)\rho_b \tag{3.14}$$

$$\frac{\partial \rho_b}{\partial t} = k_b(x)\rho_u - k_u(x)\rho_b \tag{3.15}$$

Here the additional Eq.(3.15) captures the density of the bound motors, ρ_b. And reaction fluxes are added to the diffusion equation for the binding and unbinding kinetics. The equilibrium conditions of Eqs.(3.14) and (3.15) are:

$$\frac{\partial \rho_u}{\partial x} = 0 \tag{3.16}$$

$$k_b(x)\rho_u - k_u(x)\rho_b = 0 \tag{3.17}$$

Although the density of unbound motors remains constant over space, the total density of motors, ρ_t, varies in space.

$$\rho_t(x) = \rho_u + \rho_b = \rho_u / p(x) \tag{3.18}$$

where $p(x) = k_u(x) / (k_u(x) + k_b(x))$ is the proportion of unbound motors at a given position. $p(x)$ is smaller than 1 at the substrate interface, and equals 1 elsewhere. Therefore, $\rho_t(x)$ is larger at the substrate interface than elsewhere, corresponding to clusters.

Appendix D: Energy conservation considerations

Energy conservation imposes a fundamental constraint on biophysical models. In biomechanical models, the energy reaped from biochemical reactions, e.g. ATP and ion motive force, must exceed the energy dissipated and converted by the mechanical motions. Without inertia, motions at low Reynolds number need not include kinetic energy, but the energy is typically stored as elastic potential, chemical potential or electrical potential. Our model does not include any of these elements. It only resolves the energy dissipated by the viscous drag between the motor, track, cell membrane, cell wall and substrate. The dissipated energy should be smaller than the energy provided by the proton motive force. The following arguments give a rough check on this energy constraint.

Because the model is computed with force balances, it is not obvious how much energy is consumed from the proton transfer across the membrane. Here we use the data from bacterial flagellar motor for an estimate. The stator of the flagellar motor works with stepsize ~6 nm (13.8° × 20 nm radius) (Sowa, Rowe et al. 2005; Sowa and Berry 2008) and translocates 2 protons per step (Berg 2003). Each proton provides energy around 10 k_BT. If tight coupling between stepping and proton translocation is assumed, the motor velocity is proportional to the energy consumption rate of the particular motor by a constant $2 \times 10\ k_B$T / 6nm $\approx$ 13 pN. The total energy consumption rate is then

$$\dot{E}_C = 13\,\text{pN} \cdot \sum_i V_{MH}^i \tag{3.19}$$

This is a conservative estimate for the energy consumption rate. If the motor sometimes slips, i.e. consuming protons without mechanical motion, the energy consumption rate should be even higher.

The rate of energy dissipation from all viscous drags is

$$\dot{E}_D = \zeta_C V_C^2 + \zeta_{Hrot} r \omega_H^2 + \sum_i \left(\zeta_{MB}^i V_{MB}^2 + \zeta_{MS}^i V_{MS}^2 \right) \tag{3.20}$$

Figure 3-9 shows the energy rates computed from Eqs.(3.19) and (3.20). The energy consumption rate is much larger than the resolved energy dissipation rate. Therefore, the energy conservation law has not been violated. The residue should be dissipated in the unresolved parts of the system.
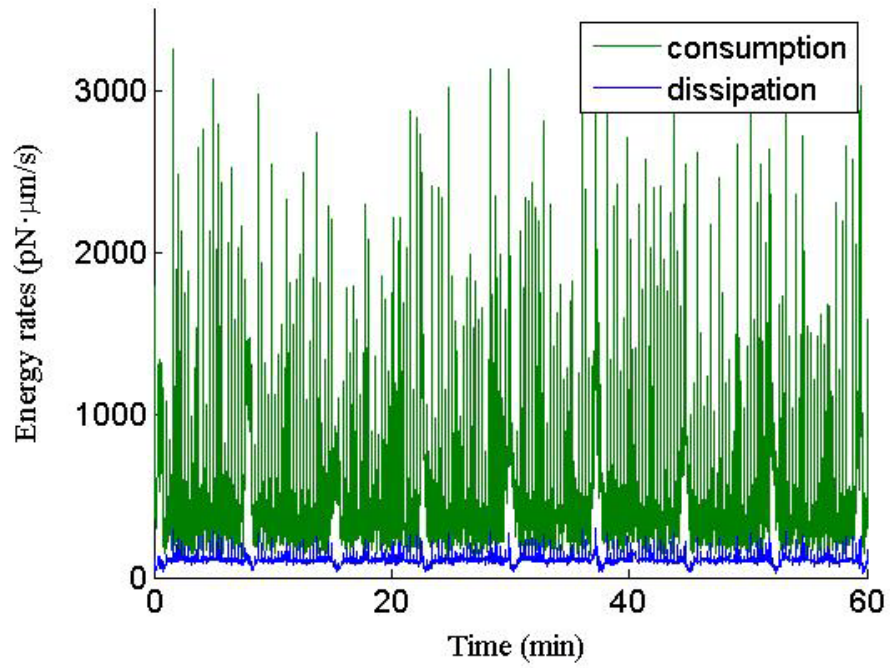
Figure 3-9: Check on energy constraint. Green line: energy consumption rate computed from Eq.(3.19); blue line: energy dissipation rate computed from Eq.(3.20). The energy dissipation rate resolved in the model is much smaller than the energy consumption rate. So the model does not violate energy conservation.

Chapter 4   Concluding Remarks

Theoretical biophysicists borrow their modeling philosophy and computational techniques from conventional theoretical physics. However, the complexity of the bacterial motility systems poses special challenges to the modeling efforts. It is often hard to define a good question in the first place, and tricky to interpret the result in the end. In this concluding chapter, I will summarize some lessons I learned from my research projects. These points are also generally true for the modeling of any complex biological systems.

As mentioned in Chapter 1, the models of bacterial motility work in close collaboration with experiments. The experimental observations thus define the appropriate level and focus of the model. As more details are revealed about the motility, more refined models become possible. For most bacteria, to start any kind of modeling it is necessary to at least have some basic structural and biophysical information. It is also helpful to learn the dynamical changes of the motility-related components while the cell is moving. For example, the earlier model for mycoplasma motility (Wolgemuth, Igoshin et al. 2003) was entirely built upon the temperature-velocity and force-velocity measurements. Since the model was born before the leg proteins were discovered, it could only explain the biophysical data with a very general biased inchworming mechanism. The issues with the Arrhenius factor were left unexplained. Our latest model, equipped with the structural information about the leg protein, was able to attribute the intriguing steep, sub-Arrhenius temperature-velocity curve to the sequential release of the substrate-binding sites on the protein. However, the work cycle of the leg protein was largely speculation based on its geometric shape and some highly generalized knowledge about ATPase motors. The lack of detailed dynamics again leaves the theory on the more general side. Instead of finding out how the particular class of bacteria move, the question has been transformed to how multi-bond adhesions rupture under different modes of pulling forces and how temperature affects the rupturing process. At the end of the day, it is quite possible, because of its generality, to find the theory suits other biological systems better than it does for mycoplasma.

By contrast, the myxobacteria system invited a much more detailed mechanical model because the double helical structure of the track leaves very narrow choices for the mode of motion. We only had to assume how symmetry breaks in the system to generate net driving force. And luckily this is clued by the dynamics of protein clusters observed in the experiments. Nevertheless, the biochemistry part is coarsened and the mechanochemical coupling left unaddressed because there is not enough information.

The right question to ask is often not obvious at the beginning of a project, especially for systems with too little information. The mycoplasma project, for example, has meandered its way through various versions with totally different angles, e.g. asymmetric elasticity in the leg, mechanochemistry of ATP hydrolysis, general system of colored noise. These models either focus on an aspect with almost no data available, like the first two, or are too general to be associated with mycoplasma at all. In the former case, the model requires too many assumptions and usually requires many unknown parameters. The large number of unknowns makes data fitting meaningless. When we finally settled on the multi-bond adhesion model, it made a good balance between generality and specificity: it incorporates the structure of the leg protein and involves only 4 unknowns. The rule of thumb is to build a model that integrates as much

experimental information as possible, and requires a small enough number of assumptions and unknown parameters.

Finally, we should be careful about what we infer from our models. The conclusions and predictions of the models stem from the assumptions. If these assumptions are ignored, one can easily misapply the conclusions, or invalidate the whole model for partial inconsistency. For example, in the biochemical part of the myxobacteria model, the Min oscillator is probably quite different from the real pathway, but regulation of the mechanics is not related to the details of the oscillation. Therefore, the theory probably remains valid in its explanation for why the polar concentration of the high-drag cargo revives at the new leading pole a short while after the cell reverses. On the other hand, even if a model is disproven with regard to its original goal, it remains a theoretical exploration about a certain form of energy conversion and transduction, signal transduction, or mechanochemical coupling. These general physical insights should not be discarded.

References

Adams, D. W. and J. Errington (2009). "Bacterial cell division: assembly, maintenance and disassembly of the Z ring." Nature Reviews Microbiology **7**(9): 642-653.

Adan-Kubo, J., A. Uenoyama, et al. (2006). "Morphology of Isolated Gli349, a Leg Protein Responsible for Mycoplasma mobile Gliding via Glass Binding, Revealed by Rotary Shadowing Electron Microscopy." J. Bacteriol. **188**(8): 2821-2828.

Alt, W. (1980). "Biased random-walk models for chemotaxis and related diffusion approximations." Journal of Mathematical Biology **9**(2): 147-177.

Anson, M. (1992). "Temperature dependence and arrhenius activation energy of F-actin velocity generated in vitro by skeletal myosin." Journal of Molecular Biology **224**(4): 1029-1038.

Bai, F., C. J. Lo, et al. (2009). "Model Studies of the Dynamics of Bacterial Flagellar Motors." Biophysical Journal **96**(8): 3154-3167.

Berg, H. C. (2003). "The rotary motor of bacterial flagella." Annual Review of Biochemistry **72**: 19-54.

Berg, H. C. and R. A. Anderson (1973). "Bacteria Swim by Rotating their Flagellar Filaments." Nature **245**(5425): 380-382.

Berg, H. C. and D. A. Brown (1972). "Chemotaxis in Escherichia coli analysed by Three-dimensional Tracking." Nature **239**(5374): 500-504.

Berg, H. C. and L. Turner (1993). "Torque Generated by the Flagellar Motor of Escherichia-Coli." Biophysical Journal **65**(5): 2201-2216.

Blair, D. F. (2003). "Flagellar movement driven by proton translocation." Febs Letters **545**(1): 86-95.

Bohm, K. J., R. Stracke, et al. (2000). "Effect of temperature on kinesin-driven microtubule gliding and kinesin ATPase activity." Febs Letters **466**(1): 59-62.

Bramkamp, M. and S. van Baarle (2009). "Division site selection in rod-shaped bacteria." Current Opinion in Microbiology **12**(6): 683-688.

Burchard, A. C., R. P. Burchard, et al. (1977). "Intracellular, periodic structures in the gliding bacterium Myxococcus xanthus." J. Bacteriol. **132**(2): 666-672.

Burchard, R. P. (1981). "Gliding Motility of Prokaryotes: Ultrastructure, Physiology, and Genetics." Annual Review of Microbiology **35**(1): 497-529.

Cameron, L. A., P. A. Giardini, et al. (2000). "Secrets of actin-based motility revealed by a bacterial pathogen." Nature Reviews Molecular Cell Biology **1**(2): 110-119.

Chambaud, I., R. Heilig, et al. (2001). "The complete genome sequence of the murine respiratory pathogen Mycoplasma pulmonis." Nucleic Acids Research **29**(10): 2145-2153.

Chen, J., J. Neu, et al. (2009). "Motor-Substrate Interactions in Mycoplasma Motility Explains Non-Arrhenius Temperature Dependence." Biophysical Journal **97**(11): 2930-2938.

Decuevas, M., T. Tao, et al. (1992). "Evidence That the Stalk of Drosophila Kinesin Heavy-Chain Is an Alpha-Helical Coiled Coil." Journal of Cell Biology **116**(4): 957-965.

Ehlers, K. M., A. D. Samuel, et al. (1996). "Do cyanobacteria swim using traveling surface waves?" Proc Natl Acad Sci U S A **93**(16): 8340-3.

Elowitz, M. B., M. G. Surette, et al. (1999). "Protein Mobility in the Cytoplasm of Escherichia coli." Journal of Bacteriology **181**(1): 197-203.

Fenimore, P. W., H. Frauenfelder, et al. (2002). "Slaving: Solvent fluctuations dominate protein dynamics and functions." Proceedings of the National Academy of Sciences **99**(25): 16047-16051.

Fischer-Friedrich, E., G. Meacci, et al. (2010). "Intra- and intercellular fluctuations in Min-protein dynamics decrease with cell length." Proceedings of the National Academy of Sciences **107**(14): 6134-6139.

Fraser, C. M., J. D. Gocayne, et al. (1995). "The Minimal Gene Complement of Mycoplasma-Genitalium." Science **270**(5235): 397-403.

Gennerich, A. and R. D. Vale (2009). "Walking the walk: how kinesin and dynein coordinate their steps." Current Opinion in Cell Biology **21**(1): 59-67.

Graumann, P. L. (2009). "Dynamics of Bacterial Cytoskeletal Elements." Cell Motility and the Cytoskeleton **66**(11): 909-914.

Henderson, G. P. and G. J. Jensen (2006). "Three-dimensional structure of Mycoplasma pneumoniae's attachment organelle and a model for its role in gliding motility." Molecular Microbiology **60**(2): 376-385.

Himmelreich, R., H. Hilbert, et al. (1996). "Complete sequence analysis of the genome of the bacterium Mycoplasma pneumoniae." Nucleic Acids Research **24**(22): 4420-4449.

Howard, J. (2001). Mechanics of Motor Proteins and the Cytoskeleton. Sunderland, Sinauer Associates, Inc.

Howard, M. and K. Kruse (2005). "Cellular organization by self-organization: mechanisms and models for Min protein dynamics." J. Cell Biol. **168**(4): 533-536.

Howard, M., A. D. Rutenberg, et al. (2001). "Dynamic Compartmentalization of Bacteria: Accurate Division in E. Coli." Physical Review Letters **87**(27): 278102.

Hyeon, C. and J. N. Onuchic (2007). "Internal strain regulates the nucleotide binding site of the kinesin leading head." Proceedings of the National Academy of Sciences **104**(7): 2175-2180.

Ivanov, V. and K. Mizuuchi (2010). "Multiple modes of interconverting dynamic pattern formation by bacterial cell division proteins." Proceedings of the National Academy of Sciences: -.

Jaffe, J., N. Stange-Thomann, et al. (2004). "The Complete Genome and Proteome of Mycoplasma mobile." Genome Research **14**(8): 1447-1461.

Jaffe, J. D., M. Miyata, et al. (2004). "Energetics of Gliding Motility in Mycoplasma mobile." J. Bacteriol. **186**(13): 4254-4261.

Jahn, E. (1924). "Beitrage zur botanischen Protistologie I. Die Polyangiden." <u>Leipzig. Geb. Borntraeger.</u>

Jing, Y., C. W. Wolgemuth, et al. (2009). "Kinematics of the swimming of spiroplasma." <u>Physical Review Letters</u>: 218102 (4 pp.).

Jones, L. J. F., R. Carballido-López, et al. (2001). "Control of Cell Shape in Bacteria: Helical, Actin-like Filaments in Bacillus subtilis." <u>Cell</u> **104**(6): 913-922.

Kaiser, D. (2003). "Coupling cell movement to multicellular development in myxobacteria." <u>Nat Rev Micro</u> **1**(1): 45-54.

Keller, E. F. and L. A. Segel (1971). "Model for chemotaxis." <u>Journal of Theoretical Biology</u> **30**(2): 225-234.

Kenri, T., S. Seto, et al. (2004). "Use of Fluorescent-Protein Tagging To Determine the Subcellular Localization of Mycoplasma pneumoniae Proteins Encoded by the Cytadherence Regulatory Locus." <u>J. Bacteriol.</u> **186**(20): 6944-6955.

Kirchhoff, H. (1992). Motility. <u>Mycoplasmas - Molecular Biology and Pathogenesis</u>. J. Maniloff, R. N. McElhaney, L. R. Finch and J. B. Baseman. Washington D.C., American Society for Microbiology**:** 289-306.

Kojima, S. and D. F. Blair (2004). The bacterial flagellar motor: Structure and function of a complex molecular machine. <u>International Review of Cytology - a Survey of Cell Biology, Vol. 233</u>. **233:** 93-134.

Kruse, T., J. Moller-Jensen, et al. (2003). "Dysfunctional MreB inhibits chromosome segregation in Escherichia coli." <u>EMBO J</u> **22**(19): 5283-5292.

Lawrence, N. H. and W. C. Richard (1971). "Gliding motility in the blue-green alga *Oscillatoria princeps* " <u>Journal of Phycology</u> **7**(2): 133-145.

Leonardy, S., G. Freymark, et al. (2007). "Coupling of protein localization and cell movements by a dynamically localized response regulator in Myxococcus xanthus." <u>Embo Journal</u> **26**(21): 4433-4444.

Lodish, H., A. Berk, et al. (2000). <u>Molecular Cell Biology</u>, Freeman & Co., New York, NY.

Macnab, R. M. (1977). "Bacterial flagella rotating in bundles: a study in helical geometry." <u>Proceedings of the National Academy of Sciences of the United States of America</u> **74**(1): 221-225.

Margolin, W. (2009). "Sculpting the Bacterial Cell." **19**(17): R812-R822.

Mauriello, E. M. F., T. Mignot, et al. (2010). Gliding Motility Revisited: How Do The Myxobacteria Move Without Flagella? (In press).

Mauriello, E. M. F., F. Mouhamar, et al. (2010). "Bacterial motility complexes require the actin-like protein, MreB and the Ras homologue, MglA." <u>EMBO J</u> **29**(2): 315-326.

Mauriello, E. M. F., B. Y. Nan, et al. (2009). "AglZ regulates adventurous (A-) motility in Myxococcus xanthus through its interaction with the cytoplasmic receptor, FrzCD." <u>Molecular Microbiology</u> **72**(4): 964-977.

Mauriello, E. M. F. and D. R. Zusman (2007). "Polarity of motility systems in Myxococcus xanthus." Current Opinion in Microbiology **10**(6): 624-629.

May, A. P., R. C. Robinson, et al. (1998). "Crystal Structure of the N-Terminal Domain of Sialoadhesin in Complex with 3' Sialyllactose at 1.85 Å Resolution." Molecular Cell **1**(5): 719-728.

Metsugi, S., A. Uenoyama, et al. (2005). "Sequence analysis of the gliding protein Gli349 in Mycoplasma mobile." BIOPHYSICS **1**: 33-43.

Mignot, T. (2007). "The Elusive Engine in Myxococcus xanthus Gliding Motility." Cell Mol Life Sci. 2007 Jul 26; [Epub ahead of print].

Mignot, T., J. Merlie, et al. (2007). "Two localization motifs mediate polar residence of FrzS during cell movement and reversals of Myxococcus xanthus." Molecular Microbiology **65**(2): 363-372.

Mignot, T., J. P. Merlie, Jr., et al. (2005). "Regulated Pole-to-Pole Oscillations of a Bacterial Gliding Motility Protein." Science **310**(5749): 855-857.

Mignot, T. and J. R. Kirby (2008). "Genetic circuitry controlling motility behaviors of *Myxococcus xanthus*." BioEssays **30**(8): 733-743.

Mignot, T., J. W. Shaevitz, et al. (2007). "Evidence That Focal Adhesion Complexes Power Bacterial Gliding Motility." Science **315**(5813): 853-856.

Miyata, M. (2005). Gliding Motility of Mycoplasmas: The Mechanism Cannot be Explained by Current Biology. Mycoplasmas: Molecular Biology, Pathogenicity and Strategies for Control. A. Blanchard and G. Browning. Wymondham, Horizon Bioscience**:** 137-163.

Miyata, M. (2007). Molecular mechanism of mycoplasma gliding - a novel cell motility system. Cell Motility. P. Lenz. New York, Springer**:** 137-175.

Miyata, M. (2008). "Centipede and inchworm models to explain Mycoplasma gliding." Trends in Microbiology **16**(1): 6-12.

Miyata, M. and J. D. Petersen (2004). "Spike structure at the interface between gliding mycoplasma mobile cells and glass surfaces visualized by rapid-freeze-and-fracture electron microscopy." J. Bacteriol. **186**(13): 4382-4386.

Miyata, M., W. Ryu, et al. (2002). "Force and velocity of Mycoplasma mobile gliding." J. Bacteriol. **184**(7): 1827-1831.

Miyata, M. and A. Uenoyama (2002). "Movement on the cell surface of the gliding bacterium, *Mycoplasma mobile*, is limited to its head-like structure." FEMS Microbiology Letters **215**(2): 285-289.

Mogilner, A. and G. Oster (2003). "Force Generation by Actin Polymerization II: The Elastic Ratchet and Tethered Filaments." Biophysical Journal **84**(3): 1591-1605.

Nagai, R. and M. Miyata (2006). "Gliding motility of Mycoplasma mobile can occur by repeated binding to N-acetylneuraminyllactose (sialyllactose) fixed on solid surfaces." Journal of Bacteriology **188**(18): 6469-6475.

Nakane, D. and M. Miyata (2007). "Cytoskeletal "jellyfish" structure of Mycoplasma mobile." Proceedings of the National Academy of Sciences of the United States of America **104**(49): 19518-19523.

Nan, B., E. M. F. Mauriello, et al. (2010). "A multi-protein complex from Myxococcus xanthus required for bacterial gliding motility." Mol Microbiol.

Ohtani, N. and M. Miyata (2007). "Identification of a novel nucleoside triphosphatase from Mycoplasma mobile: a prime candidate motor for gliding motility." Biochemical Journal **403**: 71-77.

Purcell, E. (1977). "Life at low Reynolds number." Amer. J. Physics **45**: 3-11.

Purcell, E. M. (1997). "The efficiency of propulsion by a rotating flagellum." Proceedings of the National Academy of Sciences of the United States of America **94**(21): 11307-11311.

Razin, S., D. Yogev, et al. (1998). "Molecular biology and pathogenicity of mycoplasmas." Microbiology and Molecular Biology Reviews **62**(4): 1094-1156.

Rosenfeld, S. S., P. M. Fordyce, et al. (2003). "Stepping and Stretching." Journal of Biological Chemistry **278**(20): 18550-18556.

Rosengarten, R., M. Fischer, et al. (1988). "Transport of Erythrocytes by Gliding Cells of Mycoplasma-Mobile 163k." Current Microbiology **16**(5): 253-257.

Rosengarten, R. and H. Kirchhoff (1987). "Gliding motility of Mycoplasma strain 163K." Journal of Bacteriology **169**(5): 1891-1898.

Seto, S., G. Layh-Schmitt, et al. (2001). "Visualization of the Attachment Organelle and Cytadherence Proteins of *Mycoplasma pneumoniae* by Immunofluorescence Microscopy." J. Bacteriol. **183**(5): 1621-1630.

Shaevitz, J. W., J. Y. Lee, et al. (2005). "Spiroplasma Swim by a Processive Change in Body Helicity." Cell **122**(6): 941-945.

Shih, Y.-L., T. Le, et al. (2003). "Division site selection in Escherichia coli involves dynamic redistribution of Min proteins within coiled structures that extend between the two cell poles." Proceedings of the National Academy of Sciences of the United States of America **100**(13): 7865-7870.

Skerker, J. M. and H. C. Berg (2001). "Direct observation of extension and retraction of type IV pili." Proceedings of the National Academy of Sciences of the United States of America **98**(12): 6901-6904.

Sliusarenko, O., D. R. Zusman, et al. (2007). "The Motors Powering A-Motility in Myxococcus xanthus Are Distributed along the Cell Body." J. Bacteriol. **189**(21): 7920-7921.

Soo, F. S. and J. A. Theriot (2005). "Adhesion controls bacterial actin polymerization-based movement." Proceedings of the National Academy of Sciences of the United States of America **102**(45): 16233-16238.

Sowa, Y. and R. M. Berry (2008). "Bacterial flagellar motor." Quarterly Reviews of Biophysics **41**(02): 103-132.

Sowa, Y., A. D. Rowe, et al. (2005). "Direct observation of steps in rotation of the bacterial flagellar motor." Nature **437**(7060): 916-919.

Stone, H. A. and A. D. Samuel (1996). "Propulsion of Microorganisms by Surface Distortions." Physical Review Letters **77**(19): 4102-4104.

Sun, M., M. Wartel, et al. (2010). Motor-driven Intracellular Transport Powers Bacterial Gliding Motility (submitted).

Uenoyama, A., A. Kusumoto, et al. (2004). "Identification of a 349-Kilodalton Protein (Gli349) responsible for cytadherence and glass binding during gliding of mycoplasma mobile." J. Bacteriol. **186**(5): 1537-1545.

Uenoyama, A. and M. Miyata (2005). "Gliding ghosts of Mycoplasma mobile." Proc Natl Acad Sci U S A **102**(36): 12754-12758.

Uenoyama, A., S. Seto, et al. (2009). "Regions on Gli349 and Gli521 Protein Molecules Directly Involved in Movements of Mycoplasma mobile Gliding Machinery, Suggested by Use of Inhibitory Antibodies and Mutants." J. Bacteriol. **191**(6): 1982-1985.

Wada, H. and R. R. Netz (2009). "Hydrodynamics of helical-shaped bacterial motility." Physical Review E **80**(2).

Wang, H. and G. Oster (2002). "Ratchets, power strokes, and molecular motors." Applied Physics a-Materials Science & Processing **75**(2): 315-323.

Watanabe, R., R. Iino, et al. (2008). "Temperature-sensitive reaction intermediate of F1-ATPase." EMBO reports **9**(1): 84-90.

Wolgemuth, C., E. Hoiczyk, et al. (2002). "How Myxobacteria Glide." Current Biology **12**(5): 369-377.

Wolgemuth, C. W., O. Igoshin, et al. (2003). "The motility of mollicutes." Biophysical Journal **85**(2): 828-842.

Xing, J., F. Bai, et al. (2006). "Torque-speed relationship of the bacterial flagellar motor." Proceedings of the National Academy of Sciences of the United States of America **103**(5): 1260-1265.

Xing, J., J.-C. Liao, et al. (2005). "Making ATP." Proceedings of the National Academy of Sciences of the United States of America **102**(46): 16539-16546.

Zusman, D. R., A. E. Scott, et al. (2007). "Chemosensory pathways, motility and development in Myxococcus xanthus." Nature Reviews Microbiology **5**(11): 862-872.